

# Ground motions variability in Israel from 3-D simulations of M 6 and M 7 earthquakes

Jonatan Glehman<sup>1</sup> and Michael Tsesarsky<sup>1,2</sup>

<sup>1</sup>Department of Earth and Environmental Sciences, Ben Gurion University of the Negev, 8410501, Israel

<sup>2</sup>Department of Civil and Environmental Engineering, Ben Gurion University of the Negev, 8410501, Israel

Correspondence to: Jonatan Glehman (glehman@post.bgu.ac.il)

**Abstract.** In Israel, due to low seismicity rates and sparse seismic network, the temporal and spatial coverage of ground motion data is insufficient to estimate the variability of moderate-strong ( $M > 6$ ) ground motions required to construct a local ground motion model (GMM). To fill this data gap and to study the ground motions variability of  $M > 6$  events, we performed a series of 3-D numerical simulations of M 6 and M 7 earthquakes. Based on the results of the simulations, we developed a ~~statistical~~parametric attenuation model (AM) and studied the residuals between simulated and AM PGVs and the single station variability. We also compared the simulated ground motions with a global GMM in terms of peak ground velocity (PGV) and significant duration (Ds 595). Our results ~~suggests~~suggested that the AM was unable to fully capture the simulated ground motions variability, mainly due to the incorporation of super-shear rupture and effects of local sedimentary structures. We also ~~shows~~showed that an imported GMM considerably deviates from simulated ground motions. This work sets the basis for future development of a comprehensive GMM for Israel, accounting for local sources, path, and site effects.

## 1 Introduction

The recent report by the Centre for Research on the Epidemiology of Disasters (CRED) and the UN Office for Disaster Risk Reduction (UNDRR) – Human Cost of Disasters, 2000 - 2019 – clearly shows that earthquakes are the deadliest natural disasters. ~~Counting~~Accounting for only 3 % of the total number of people affected by natural disasters, they count for 58 % of deaths (more than 700,000) of all disaster types and 21 % of recorded economic losses (Mizutori and D’ebarati, 2020). Over the past 40 years, the global population exposed to a moderate to severe intensity earthquake has increased by 93 % (to 2.7 billion people) (Pesaresi et al., 2017). This value is expected to grow with population growth and increasing urbanization.

Seismic hazard is the intrinsic natural occurrence of earthquakes and the resulting ground motion and other effects (Wang, 2005). Ground motion models (GMM’s) are critical components in the mitigation of seismic hazard. Empirically based GMMs, also known as Ground Motion Prediction Equations (GMPE’s), are parametric models that estimate the median and the variability of the expected ground motions at a site. The main explanatory variables of such models are typically earthquake magnitude, distance, and site conditions. New generation ~~GMPEs~~GMMs also address faulting style, depth to rock, and others.

Many regions worldwide, either due to low seismicity rates and/or sparse coverage of the seismic network, do not provide sufficient temporal and spatial data to estimate the variability of ground motions required to construct a local ~~GMPE~~GMM or validate an imported ~~GMPE~~GMM to local conditions. This situation is specifically acute in the range of strong earthquakes at relatively short distances that pose the most significant hazard to human life and infrastructure.

37 The use of imported ~~GMPE's~~GMM's under the ergodic assumption attributes the ground motion variability  
38 to the randomness of the process (i.e., aleatory variability) rather than to local systematic source-path and site  
39 effects (i.e., epistemic uncertainty) (Anderson and Brune, 1999). Abrahamson et al., (2019) showed that the  
40 increased number of strong-motion records over the past decade exhibit significant differences in scaling of the  
41 ground motions even within relatively small regions and that most of the variability typically treated as aleatory  
42 is actually due to systematic source, path, and site effects. Kuehn et al., (2019) showed the importance of variations  
43 in quality factor (Q) over small spatial scales (30 km) in California. Specifically showing that accounting for path  
44 effects leads to a smaller value of the aleatory variability and results in different median predictions, depending  
45 on source and site location. To achieve this improvement, Kuehn et al., (2019) divided California into a grid with  
46 a cell size of 30 km by 30 km and used 12,039 records from 274 events recorded at 1504 stations. This approach  
47 can be employed only in data-rich regions, such as California. Lan et al., (2019) showed that for South Western  
48 China, imported ~~GMPE's~~GMM's result in significant discrepancies compared with regional instrumental data  
49 (including the Wenchuan Mw 7.9 event). In addition, despite the recorded ground motion data expanding, it  
50 remains sparse for large, complex ruptures with recurrence intervals generally exceeding the observation length  
51 of instrumental records.

52 The challenges met while predicting ground motion in data-poor regions turn numerical modeling into an  
53 essential complementary method for seismic hazard analysis (Chaljub et al., 2010). Numerical modeling alleviates  
54 the need for the ergodic assumption, as it can augment the seismic data with strong motion records and account  
55 for ground motions variability by systematically separating source, path, and site effects. For example, Graves et  
56 al., (2011) showed that the combination of rupture directivity and basin response effects could lead to an increased  
57 hazard in particular sites, relative to that calculated by ~~GMPE~~GMM. Pitarka et al., (2021) found that the  
58 combination of rupture propagation effects with the amplification due to local topography can result in large  
59 ground motions amplifications with complex spatial variability.

60 However, the shift from ergodic models to nonergodic models, which account for local source-site and  
61 path effects such as numerical models, leads to large epistemic uncertainty in the median ground motion, resulting  
62 in increased epistemic uncertainty of the hazard (Walling & Abrahamson, 2012). Such uncertainty ~~is derived~~  
63 from both modeling and parametric uncertainties, as the model is not well constrained. ~~However, m~~Model  
64 uncertainty can be reduced by using more accurate 3D crustal models and source models.

65 Subsurface models with different levels of accuracy and completeness, are available ~~for other parts~~  
66 ~~of around~~ the world. With the increasing use of terrestrial and space geodesy, the control of seismic sources is also  
67 improving with time. Combining the two enables the construction of numerical models for regional assessment  
68 of ground motions (Douglas & Aochi, 2008; Graves & Pitarka, 2015; Pitarka et al., 2021). A hybrid GMM, based  
69 on empirical and synthetic ground motion databases, is expected to reduce the epistemic uncertainty of the median  
70 ground motion and will lead to a lower aleatory variability than ~~GMM's based on data with limited magnitude and~~  
71 ~~distance bands, magnitude limited GMPE's~~.

72 In Israel, low seismicity rates (centennial and millennial return periods) and a limited instrumental catalog,  
73 ~~spanning~~ only four decades and contain mainly  $M < 6$  events, impede the development of local empirical GMM.  
74 The practical outcome of this shortcoming is the use of imported GMM's, such as the Campbell & Bozorgnia,  
75 (2008; ~~hereafter, CB08~~) used in the Israel Seismic Design Code IS 413 (Israel Standards Institution, 2013).  
76 Contrary to the instrumental catalog, the Israel pre-instrumental catalog spans over three millennia (Agnon, 2014),

77 including numerous  $M > 6$  events, with up to 14  $M > 7$  events. ~~In addition, recent geodetic studies (Hamiel et al.,~~  
78 ~~2016; Sadeh et al., 2012) identified a slip deficit on specific segments of the Dead Sea Transform (DST) equivalent~~  
79 ~~to an  $M > 7$  earthquake.~~

80 This paper presents numerical modeling of ground motions in Israel, intended to ~~narrow the strong ground~~  
81 ~~motion data gap and~~ study ground motions variability from moderate ( $M 6$ ) and strong ( $M 7$ ) earthquakes. The  
82 primary purpose of this work was to study the different source, path, and site effects of simulated  $M 6$  and  $M 7$   
83 earthquakes and their contribution to ground motion variability in Israel. To this end, we have improved the 3-D  
84 regional velocity model of Shimony et al., (2021) and numerically modeled  $M 6$  and  $M 7$  earthquakes with  
85 different source and path properties. Following, we developed a parametric model of median ground motions and  
86 their variability in terms of Peak Ground Velocity (PGV). The model quantifies the spatial distribution of the  
87 ground motions in central and northern Israel, accounting for source, path, and site effects.

88 We begin with a brief introduction to the seismo-tectonic setting of the region. Then, we proceed to the  
89 methodology section to describe the process of generating a synthetic ground motion database and the subsequent  
90 construction of a ~~statistical~~parametric ground motion model. Next, the results section, we present the simulated  
91 ground motions and the respective attenuation model. Then, ~~we show the comparison between the results of our~~  
92 ~~simulations compares it with the and~~ global ~~GMPE's~~GMM's of Campbell & Bozorgnia, (2014; hereafter, CB14)  
93 and Afshari & Stewart, (2016) ~~performance with respect to the synthetic database.~~ Finally, we discuss our findings  
94 and provide insights regarding the seismic hazard from moderate to strong earthquakes and the importance of  
95 developing a ~~comprehensive~~ regional GMM to mitigate the seismic hazard in Israel.

## 96 **2 The seismo-tectonic setting of Israel**

### 97 **2.1 Seismicity and seismic hazard in Israel**

98 The Dead Sea Transform (DST) fault system is an active tectonic boundary separating the African and Arabian  
99 plates. Extending from the Gulf of Aqaba to southern Turkey, a total length of ~~ea~~approx. 1100 km, it dominates  
100 the seismicity of Israel, Palestinian Authority, Lebanon, and Syria (Fig. 1a,b). The DST is a left-lateral strike-slip  
101 fault with a total offset of 105 km (Garfunkel, 2014). The average long-term slip rate is 4 to 5 mm year<sup>-1</sup> (Bartov  
102 et al., 1980). Geodetic slip rates along the ~~Israel~~Israeli part of the DST ~~ranges~~range from 3 to 5 mm year<sup>-1</sup> (Hamiel  
103 et al., 2016; Sadeh et al., 2012).

104 Splaying north-west from the DST is the Gilboa Fault, and farther north-west towards the Mediterranean,  
105 the Carmel Fault. Both comprise an active zone generalized as the Carmel Fault Zone (CFZ). The DST segments  
106 are capable of producing  $M 6$  and  $M 7$  ~~7.5~~7.5 events (Shamir et al., 2001; Hamiel et al., 2009), and the CFZ is capable  
107 of producing up to  $M > 6.5$  earthquakes (Grünthal et al., 2009).

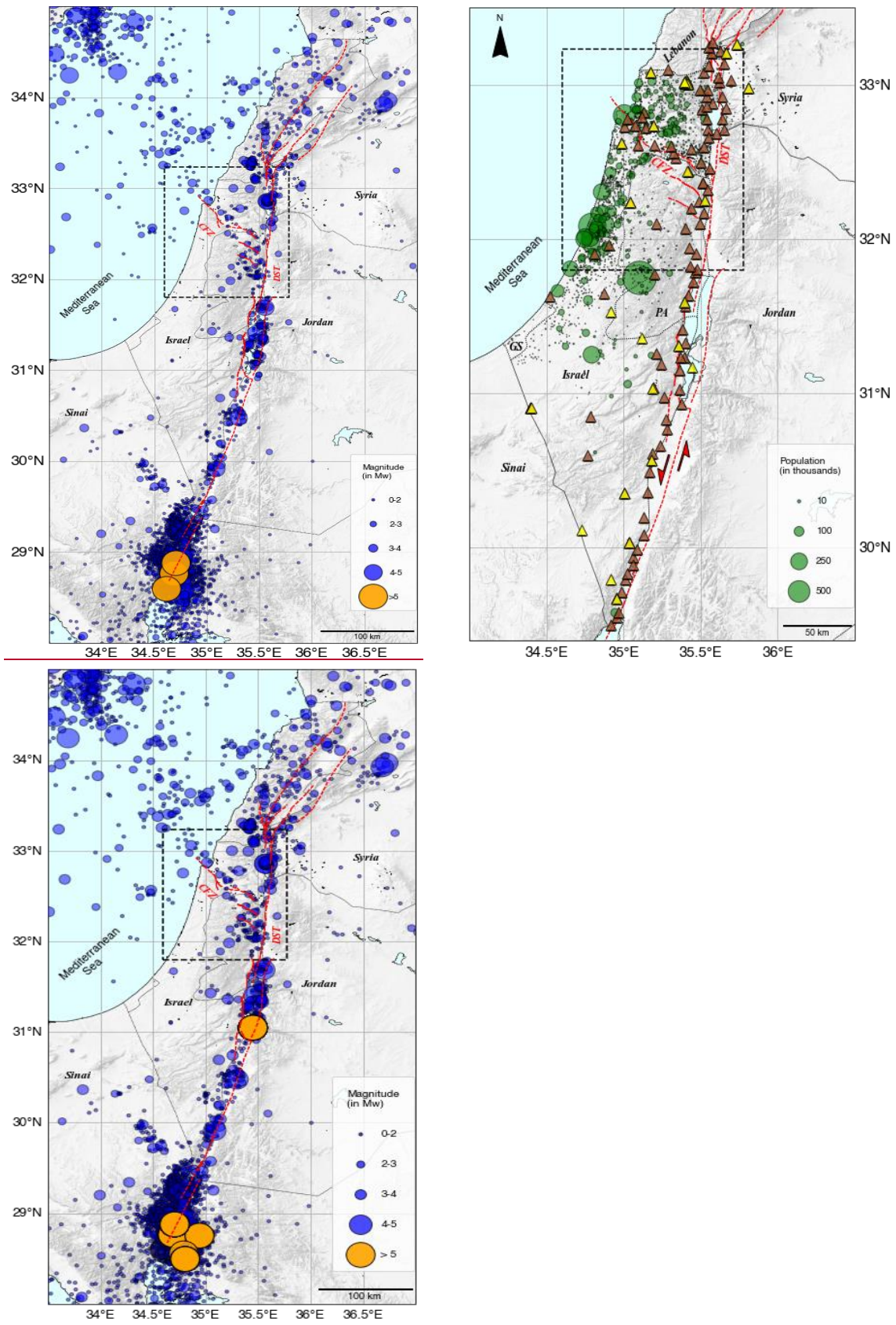
108 The Israel Seismic Network (ISN), established in 1983 and upgraded over the years, consists of a mixture  
109 of different instrumental and operational stations, including short-period stations (~~2414~~2414 in total), broadband  
110 stations (~~4424~~4424 in total), and a large broadband array (part of the Comprehensive Nuclear Test Ban Treaty). The  
111 deployment of the ISN does not cover areas of increased seismic hazard, e.g., densely populated zones and soil  
112 sites, or areas designated by the Israel Seismic Code (IS413) as suspected in extreme ground motion amplification,  
113 such as the Zevulun Valley (Fig. 1b). Currently, the seismic network is upgraded within the ~~Tru'a~~TRUAA project  
114 (an early warning system), with up to ~~6069~~6069 strong-motion accelerometers and 12 broadband seismometers added

115 to ISN (Kurzon et al., 2020). However, most of the instrumentation ~~will be~~ placed along the DST and Carmel  
116 fault to provide early warning, and not in densely populated or industrialized areas where the seismic risk is  
117 tangible. Based on demographic projections (the Taub Center for Social Policy Study in Israel; [For URL see data](#)  
118 [and resources](#)) the population of Israel is expected to grow from 9.05 million in 2021 to 12.8 million in 2040 and  
119 combined with the increasing demand for housing and infrastructures, the seismic risk is expected to grow.

120 The Israel seismic catalog covers 36 years of measurements (1985–2021) and includes more than 23,300  
121 events (Wetzler & Kurzon, 2016), but only 15 of them are of  $M > 5$  (Fig. 1a and Fig. 2). Moving back in time,  
122 Israel's pre-instrumental catalog spans over 3000 years (Agnon, 2014; Zohar, 2019) with many catastrophic  
123 events, such as the 749 ( $M > 7$ ), 1202, ( $M > 7.5$ ), 1759 ( $M > 7$ ), and the 1837 ( $M > 7$ ) earthquakes, among others.  
124 In total, fourteen  $M > 7$  events were cataloged by Ambraseys (2006) in the past two millennia. Recent geodetic  
125 studies (Hamiel et al., 2016; Sadeh et al., 2012) identified a slip deficit on specific segments of the DST, such as  
126 the Jordan Gorge Fault (JGF) and the Jordan Valley Fault (JVF), equivalent to an  $M > 7$  earthquake.

(a)

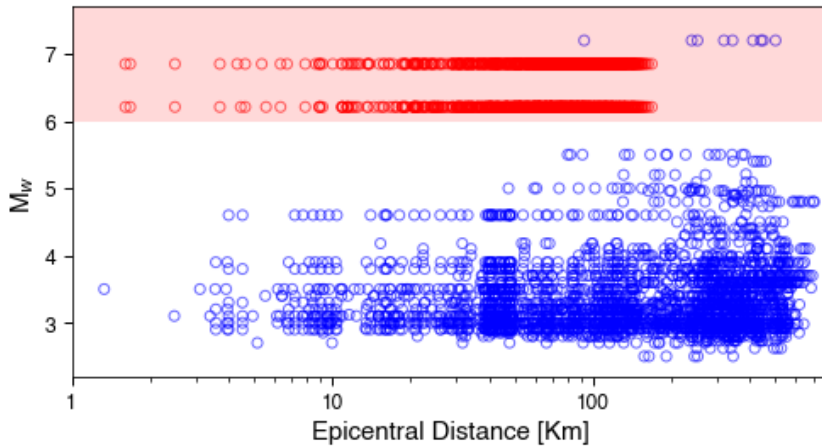
(b)



127 **Figure 1.** (a) Israel Seismic catalog (Mw) for the period 1985-2021 orange circles are events with Mw > 5 (expansion of  
 128 Wetzler & Kurzon (2016) catalog). Red lines are active tectonic borders and faults, DST is Dead Sea Transform, CFZ is  
 129 Carmel Fault Zone. (b) Demographics of Israel and the Palestinian Authority (PA) and the deployment of the Israel Seismic



130 Network. Yellow triangles are the old (up to October 2017) Israel Seismic network stations, brown triangles are the current  
 131 (~~TRUA~~TRUAA) seismic network stations. (after (Kurzon et al., 2020)). GS is Gaza Strip. The black rectangles define the  
 132 computational domain presented in Fig. -3a.



134 **Figure 2.** Israel's ground motion database (blue circles) for the period 1983-2021 as a function of epicentral distance (Yagoda-  
 135 Biran et al., 2021). The shaded rectangle spans the  $M_w > 6$  region of moderate-strong ground motion records. The red circles  
 136 are the simulated ground motions from this work.  
 137

## 138 2.2 Spatial heterogeneity of Israel

139 The geological structure of Israel exhibits strong spatial heterogeneity over short scales (Fig. 3a,b). Deep pull-  
 140 apart basins (up to 10 km) filled with soft sediments ( $V_s \sim 600\text{-}800$  m  $\text{sec}^{-1}$ ) accompany the active DST system,  
 141 from south to north: The Dead Sea Basin, Beit Shean Valley (BSV), the Sea of Galilee (SG) and the Hula Valley  
 142 (Rosenthal et al., 2019). Along the CFZ, the Zevulun, Harod, and Jezreel Valleys are formed. The vulnerability  
 143 of Zevulun Valley is particularly crucial because of its dense population and the high concentration of strategic  
 144 industrial infrastructure (Shani-Kadmiel et al., 2020).

145 The Israeli coastal plain ~~is~~ one of the most densely populated regions of the country (on average, 9000  
 146 people per  $\text{km}^2$ ), is underlain by a westward thickening sedimentary wedge (SW). In the Judea foothills area, east  
 147 of the SW, a strong reflector exists between the sandstones and clays (Pleistocene Kurkar Gr,  $V_s \sim 300$  m  $\text{sec}^{-1}$ )  
 148 and the hard carbonate rocks (the Cretaceous Judea Group,  $V_s \sim 2000$  m  $\text{sec}^{-1}$ ). In the coastal plain, the Kurkar  
 149 Group overlays the soft carbonates (Avedat Gr,  $V_s \sim 900$  m  $\text{sec}^{-1}$ ) and clastic sediments (the Bet Guvrin Fm.,  $V_s$   
 150  $\sim 800$  m  $\text{sec}^{-1}$ ) (refer to Fig. 3b). The depth of the Kurkar Group base reflector is typically several tens of meters.  
 151 Further to the west, a prominent reflector is a contact between the clays (Pliocene Yafo Fm.,  $V_s \sim 600$  m  $\text{sec}^{-1}$ )  
 152 and top of Judea Group (Gvirtzman et al. 2008). These two reflectors, when shallower than 250 m, were used  
 153 for the latest update of the Israel Building Code IS 413 (Israel Standards Institution, 2013) to ~~delimit~~delineate  
 154 areas of high potential of ground motion amplification (Gvirtzman and Zaslavsky, 2009). This situation further  
 155 complicates the process of developing an empirical ~~new-generation~~GMM for Israel.

## 156 2.3 Source effects

157 The impact of inter-basin sources along the DST on regional ground motions was examined by Shimony et al.,  
 158 (2021). This work clearly showed that regional ground motions are determined by source-path coupling effects in

159 the strike-slip basins before waves propagate into the surrounding areas. Ground motions are determined by the  
160 location of the rupture nucleation, the near-rupture lithology, and the local structures. Shimony et al., focused on  
161 symmetric sub-shear ruptures and did not model rupture directivity or super-shear rupture velocities, both known  
162 to amplify regional ground motions.

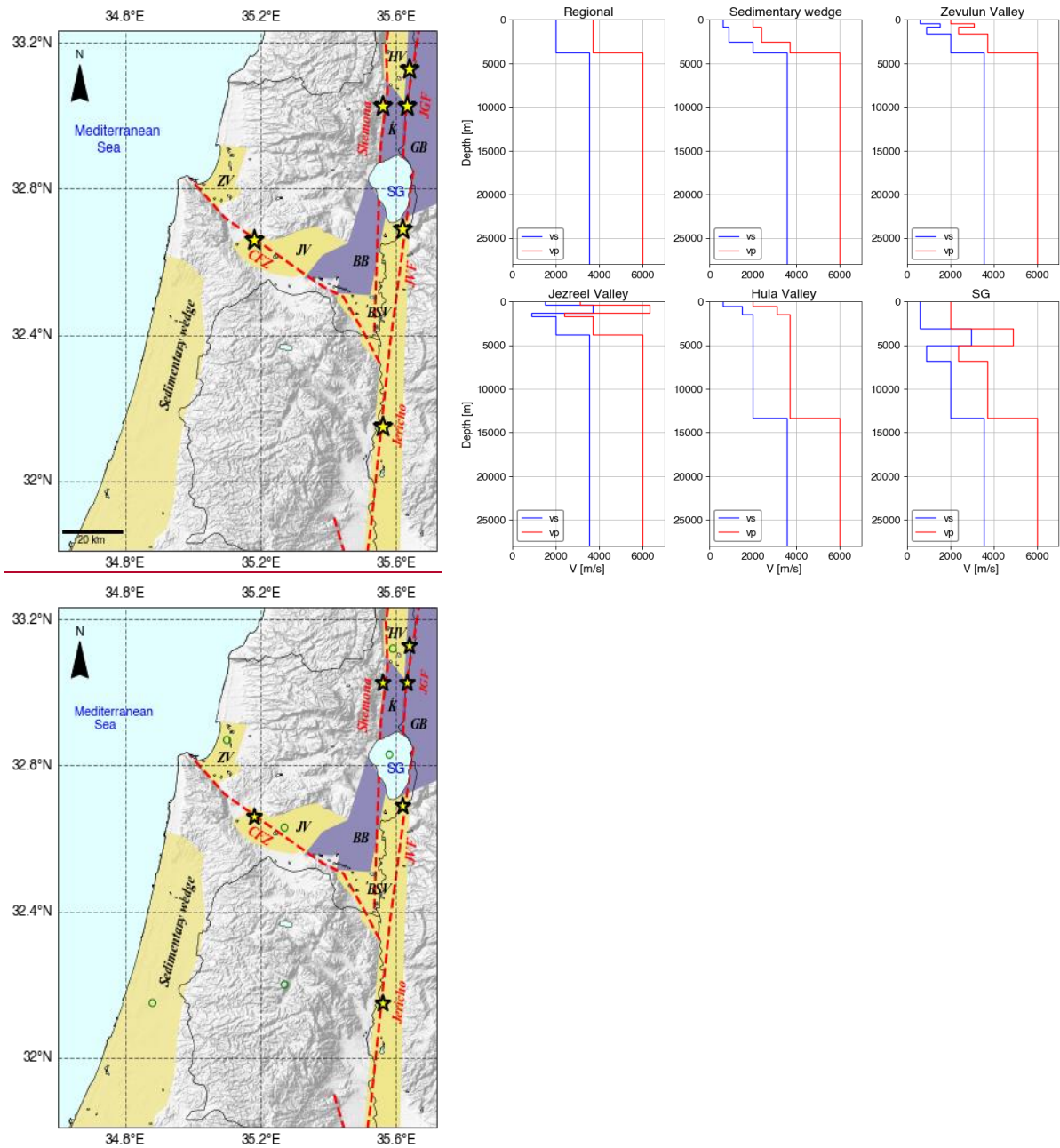
163 Under specific conditions, super-shear ruptures and directivity occur on bi-material faults (Shi & Ben-Zion  
164 2006). Specifically, for subsonic propagation, symmetrically initiated bilateral rupture evolves after some  
165 propagation distance to a unilateral rupture in the positive direction, which is the direction of slip on the compliant  
166 side of the fault containing the softer layer. The magnitude of this effect increases with propagation velocity and  
167 the degree of material contrast across the fault. At super-shear propagation speeds, along a bi-material fault, the  
168 propagation direction is reversed.

169 The DST is a mature left-lateral fault with a 105 km offset, resulting in strong material contrast between  
170 the hard layers on the Jordan side (east) and the soft layers on the Israeli side (west). Thus, the ~~rupture~~rupture can  
171 potentially propagate unilaterally southwards, discharging most of the seismic energy into Israel or northward in  
172 super-shear mode. The Jordan Gorge Fault and the Jordan Valley Fault (both active faults of the DST) specifically  
173 can produce an earthquake with ~~rupture~~rupture propagating in super-shear velocity since they border deep  
174 sedimentary basins, characterized by large shear wave velocities contrast along the ~~rupture~~rupture propagation  
175 path. Thus, to quantify the seismic hazard ensuing from bi-material faults, it is necessary to study the two  
176 propagation directions: both sub-shear and ~~super~~super-shear velocities.

177 ~~The primary purpose of this study work is was to study the examine different source path and site effects~~  
178 ~~of simulated, moderate M 6 and moderate strong M 7 earthquakes and their contribution to ground motion~~  
179 ~~variability in Israel. To this end, we have improved the 3-D regional velocity model of Shimony et al., (2021) and~~  
180 ~~numerically modeled simulated M 6 and M 7 earthquakes with different source and path properties.~~  
181 ~~ThenFollowing, we developed a parametric model statistical representation of median ground motions and their~~  
182 ~~variability. Formulated in terms of Peak Ground Velocity (PGV). Theour model quantifies the spatial distribution~~  
183 ~~of the ground motions in central and northern Israel, accounting for local source, path, and site effects, including~~  
184 ~~rupture velocity and directivity.~~

(a)

(b)



185 **Figure 3.** (a) The DST fault system and the Carmel Fault Zone (CFZ) and accompanying structures. Sedimentary structures  
 186 (yellow): BSV-Beit Shean Valley, ZV-Zevulun Valley, JV-Jezreel Valley, HV-Hula Valley, SG-Sea of Galilee, and the  
 187 Sedimentary wedge; and hard rock structures (purple): K-Korazim structural saddle, BB-Belvoir Basalts, GB-Golan Basalts;  
 188 and the Sedimentary wedge. The yellow stars indicate the epicenter of the seismic sources simulated in our work: Jordan Gorge  
 189 Fault (JGF), with bilateral and unilateral slip realization, Jordan Valley Fault (JVF), Jericho Fault, Shemona Fault (only for M  
 190 7), and CFZ (only for M 6). (b) Representative depth velocity profiles of the computational domain- (green circles).

### 191 3 Methodology and workflow

192 Developing a regional GMM for Israel requires a database of ground ~~motions~~ motion records, including  $M > 6$   
 193 events at short,  $<100$  km, distances. To supplement the existing ground motions database, we added a suite of  
 194 synthetic ground motions from physics-based 3D numerical models of different M 6 and M 7 earthquakes (Fig.  
 195 2).



196 Our work comprised two main stages; first, we ~~developed~~modified and expanded the regional velocity  
197 model of Shimony et al., (2021), ~~following to represent a more realistic geological setting and contain the Golan~~  
198 ~~Basalts, the central part of Israel, and the sedimentary wedge. Then,~~ we simulated five different earthquake  
199 scenarios for each magnitude, with nucleation at different locations along the DST and CFZ. For each scenario,  
200 we recorded synthetic ground motions at 129 stations (see supplementary material, Fig. S1), ~~with 124 stations~~  
201 ~~deployed in a uniform grid with 10 km spacing and five more stations in areas of interest (such as Zevulun Valley,~~  
202 ~~Kiryat Shemona, among others).~~ Next, we performed a ~~statistical~~ analysis ~~of~~ the synthetic database, ~~using~~  
203 ~~multivariable regression,~~ by minimizing residuals between data and model estimations. We then formulated a  
204 ~~statistical parametric~~ model of the ground motions and examined ~~its consistency with the simulated database, in~~  
205 ~~terms of the median ground motions and their variability for each of the simulated scenarios.~~

### 206 3.1 Numerical model

207 Ground motions in this research were modeled using the SW4v2 software (Petersson and Sjogreen, 2014, 2017a,  
208 b), developed for large-scale simulations of seismic wave propagation on parallel computers.

209 The velocity model covers the northern and central part of Israel (fig. 4a) and includes the main DST trough  
210 and the following basins/structures, from south to north: Beit Shean Valley (BSV), Belvoir Basalts (BB), Sea of  
211 Galilee (SG), Korazim structural saddle (K), Golan Basalts (GB) and Hula Valley (HV). Along the CFZ, we model  
212 the major sedimentary basins of Jezreel Valley (JV) and Zevulun Valley (ZV). The coastal plain is underlain by  
213 the westward thickening Sedimentary wedge (SW). Geographically, the model extends from the city of Ashdod  
214 in the south (31.8° N, 34.6° E) to Hula Valley in the north (33.23° N, 35.72° E) and from the Mediterranean Sea  
215 in the west to the Golan Basalts in the east. Figures 4b,c,d illustrate the north-south and east-west cross-sections  
216 of the velocity profiles. The numerical domain spans 159 km in the north-south direction and 124 km in the east-  
217 west direction. It covers almost 80 % of the Israeli population and a significant part of the population of the  
218 Palestinian Authority.

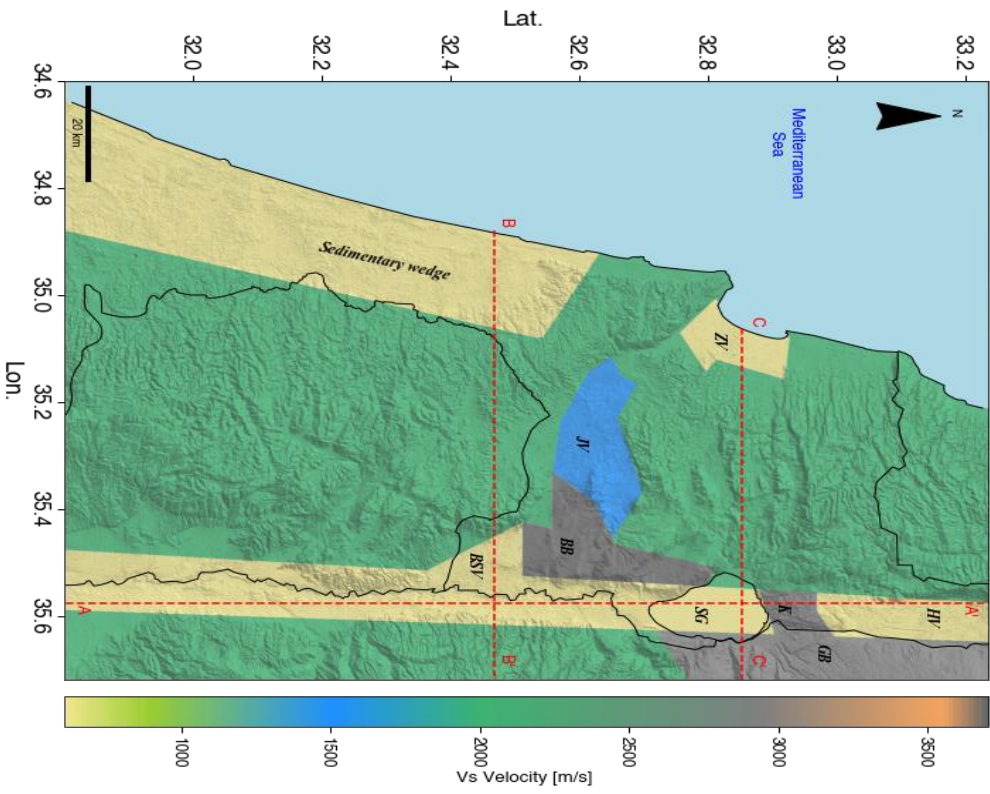
219 Subsurface geometry and the characteristics of the DST trough were obtained from Rosenthal et al., (2019)  
220 with modifications for the Hula Valley, obtained from the density log of the Notera 3 (Rybakov et al., 2003). The  
221 sedimentary wedge structure retrieved from Gvirtzman et al. (2008) and the Zevulun Valley structure was set  
222 using data from Gvirtzman et al. (2011). The basement depth along the model is based on Ben-Avraham et al.,  
223 (2002). ~~Five~~ physical quantities describe the viscoelastic material model used in this research: shear wave  
224 velocity ( $V_s$ ), pressure wave velocity ( $V_p$ ), density ( $\rho$ ), and seismic quality factors ( $Q_s$ ,  $Q_p$ ) for each point in the  
225 computational space. The missing parameters were assessed indirectly by using the correlation presented by  
226 Brocher (2008). The main units with their respective velocity, density and quality factors are shown in Table 1.

227 Seismic sources were modeled using the distributed slip model (DSM) developed by Shani-Kadmiel et al.,  
228 (2016). DSM is a kinematic model which describes the rupture patch as an elliptic surface with maximum slip at  
229 the nucleation point, decaying toward the edges as a pseudo-Gaussian function (Fig. S2). Shani-Kadmiel et al.,  
230 (2016) present validation of the DSM using macroseismic reports of the 1927 Jericho earthquake, showing good  
231 agreement between the reported and simulated ground motions. Rupture patch size and displacements were scaled  
232 following the relations presented in Wells & Coppersmith (1994). All sources were modeled as left-lateral, vertical  
233 strike slips (a dip of 90° and rake of 0°), with a strike of 3° for sources on the DST and a strike of 325° for the

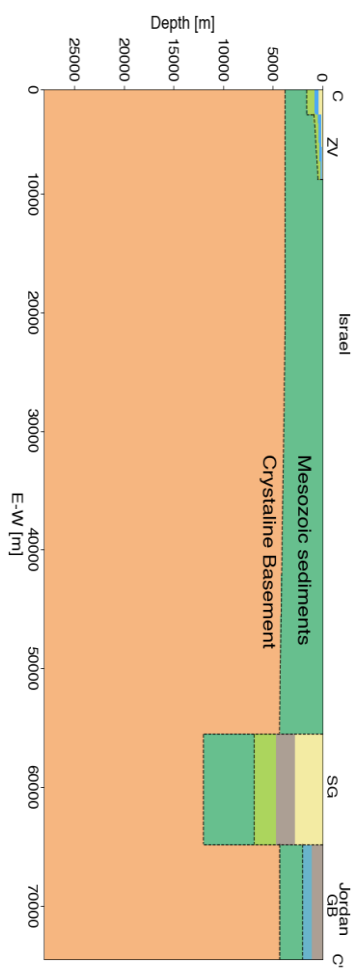
234 CFZ. The moment-rate time function of each point on the rupture patch was set to a GaussianInt pulse (Petersson  
235 and Sjogreen, 2017b) with a central frequency of  $f_0=0.4$  Hz and a maximum frequency of  $f_{\max}=1$  Hz.

236 The depth of the model was set to 28 km corresponding to the maximum seismogenic depth in this region  
237 (Wetzler and Kurzon, 2016). We assigned a minimum shear wave velocity of  $608 \text{ m s}^{-1}$  for the uppermost  
238 sedimentary layer due to the computational limitations of our system. Grid spacing was set to 76 m in accordance  
239 with the minimum shear wave velocity and the maximum frequency of the source. We set the simulation time to  
240 120 seconds to allow the slowest waves to propagate across the entire computational domain. The main parameters  
241 of the numerical setting are summarized in Table 2.

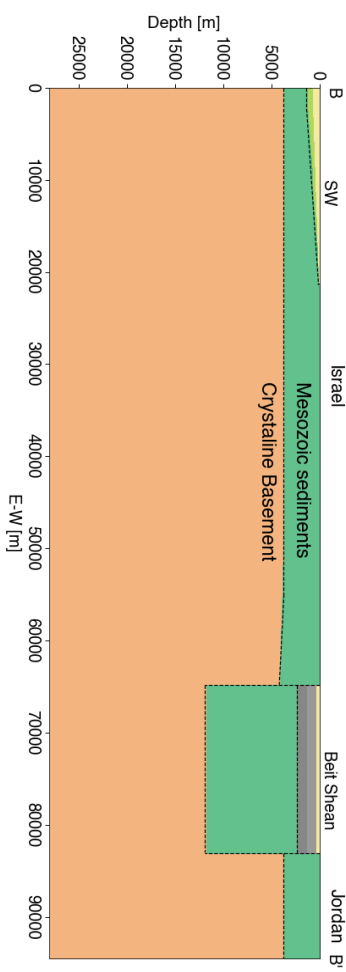
(a)



(b)



(c)



(d)

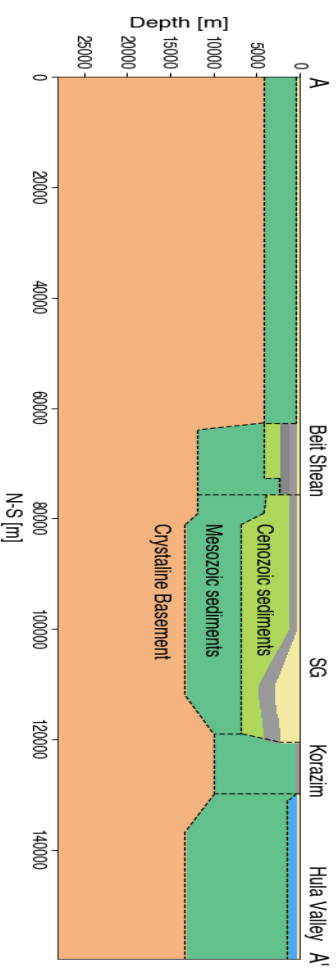


**Figure 4.** (a) The numerical model of the computational domain accompanied with subsurface cross-sections, marked with red dashed lines: (b) east-west cross section through Zevulun Valley, CC' (c) east-west cross-section through the Sedimentary wedge, BB' and (d) north-south cross-section through the DST trough, AA'.

**Table 1.** Material properties of main stratigraphic units used in this work

Model part	Rock Formation	Vs [m s <sup>-1</sup> ]	Vp [m s <sup>-1</sup> ]	Qs	Qp	ρ [Kg m <sup>-3</sup> ]
Regional	Crystalline basement	3550	6000	403	806	2720
	Cenozoic and <del>Senonian</del> Mesozoic sediments (Judea/ Talme Yafe, Mount Scopus Avedat, and Lower Saqiye)	2000	3700	160	320	2350
Local variations:						
DST	Cenozoic sediments (Umm Sabune, Bira and Gesher)	887	2380	62	124	2054
	Miocene volcanics (lower basalt)	3698	6330	439.5	879	2790
	Pliocene volcanics (upper basalt)	2947	4900	282	564	2520
	Notera/Lisan	608	2000	39.87	79.74	1900
Hula	Cenozoic sediments	1500	3100	111.5	223	2245
	Notera/Lisan	608	2000	39.87	79.74	1900
JV	Cenozoic sediments (Umm Sabune, Bira, and Gesher)	887	2380	62	124	2054
	Miocene volcanics (lower basalt)	3698	6330	439.5	879	2790
	Cenozoic sediments	1500	3100	111.5	223	2245
ZV	Cenozoic and Senonian sediments (Mount Scopus Avedat and Beit Guvrin)	887	2380	62	124	2054
	Cenozoic sediments (Patish)	1500	3100	111.5	223	2245
	Cenozoic sediments (Kurkar and Yafo)	608	2000	39.87	79.74	1900
SW	Cenozoic sediments (Lower Saqiye)	887	2380	62	124	2054
	Cenozoic sediments (Kurkar and Upper Saqiye)	608	2000	39.87	79.74	1900

**Table 2.** Main parameters of the numerical model

Parameters	Value
Model Dimensions (L×W×D)	159.63 Km × 124.45 Km × 28 Km
Spatial spacing (dh)	76 m
Grid size (points)	1.27 × 10 <sup>9</sup>
Time step spacing	0.0125 s
Simulated time	120 s
Source Dimensions (L×D)	M 6: <del>4.632</del> Km × <del>8.515</del> Km
	M 7: <del>4.938</del> Km × <del>8.522</del> Km
Source maximum and average slip	M 6: 0.5 and 0.2 m
	M 7: 3 and <del>1.357</del> m
Seismic moment (M <sub>0</sub> )	M 6: 2.57 × 10 <sup>18</sup> N·m (Mw 6.21)
	M 7: 2.37 × 10 <sup>19</sup> N·m (Mw 6.85)
Source fundamental (f <sub>0</sub> ) and maximal frequencies (f <sub>max</sub> )	0.4 and 1 Hz

245 **3.2 Earthquake scenarios and database**

246 To examine the variability of ground motions from moderate M 6 and strong M 7 earthquakes, we concentrated  
 247 on earthquake events nucleating on active segments of the DST system, with known slip deficit, and along the  
 248 CFZ. We modeled a symmetric bilateral rupture on the Jordan Gorge Fault (JGF-B), Jericho Fault (JF) Carmel  
 249 Fault Zone (CFZ) and the Shemona Fault (SF), a southward unilateral rupture on the JGF (JGF-U), and a super-  
 250 shear rupture on the Jordan Valley Fault (JVF) (Fig. 3).

251 The hypocenter for the DST events was placed in the middle of the seismogenic depth; 11 and 13 Km, for  
 252 the M 6 and M 7 respectively, for the M 6 CFZ, the value was set to 12 Km. The rupture patch was designed to  
 253 be contained in uniform lithology to prevent super-shear rupture speeds in the shallow parts of our model.  
 254 Therefore, rupture speed for each scenario was set to 0.9  $V_S$  of the lithology surrounding the nucleation zone. The  
 255 only exception was the JVF scenario for both M 6 and M 7, in which we modeled super-shear effects. For this  
 256 scenario, the rupture nucleates within the hard rock with a sub-shear speed of 1800 m s<sup>-1</sup> and evolves into  
 257 supershear rupture when it ruptures the sediments with shear wave velocity of <900 m s<sup>-1</sup>. The rupture velocity of  
 258 each scenario corresponds to the local variations of the sediment's depth. Following the transition of the nucleation  
 259 zone from the shallow crystalline basement in the south and west parts of the model to the thick Mesozoic and  
 260 Cenozoic sediments in the north and the east, the rupture velocity decreases from 3195 m s<sup>-1</sup> along the Shemona,  
 261 Carmel, and Jericho faults to 1800 m s<sup>-1</sup> along the JGF and JVF faults. As a reference, we simulated a simple two-  
 262 layered reference model (Ref) on the JGF, with mechanical properties similar to the regional setting, following  
 263 Aldersons et al., (2003). The scenarios are summarized in Table 3.

264 **Table 3.** Earthquake scenarios

Fault Name	Scenario	Magnitude (M)	Rupture speed (m s <sup>-1</sup> )	Hypocentral depth (Km)
Jordan Gorge	Bilateral rupture (JGF-B)	6, 7	1800	11 and 13
Jordan Gorge	Southward unilateral rupture (JGF-U)	6, 7	1800	11 and 13
Jordan Valley	Bilateral super-shear rupture (JVF)	6, 7	1800	11 and 13
Jericho	Bilateral rupture (JF)	6, 7	3195	11 and 13
Shemona	Bilateral rupture (SF)	7	3195	13
Carmel	Bilateral rupture (CFZ)	6	3195	12
Reference	Bilateral rupture (Ref)	6, 7	3195	11 and 13

265 **4 Results**

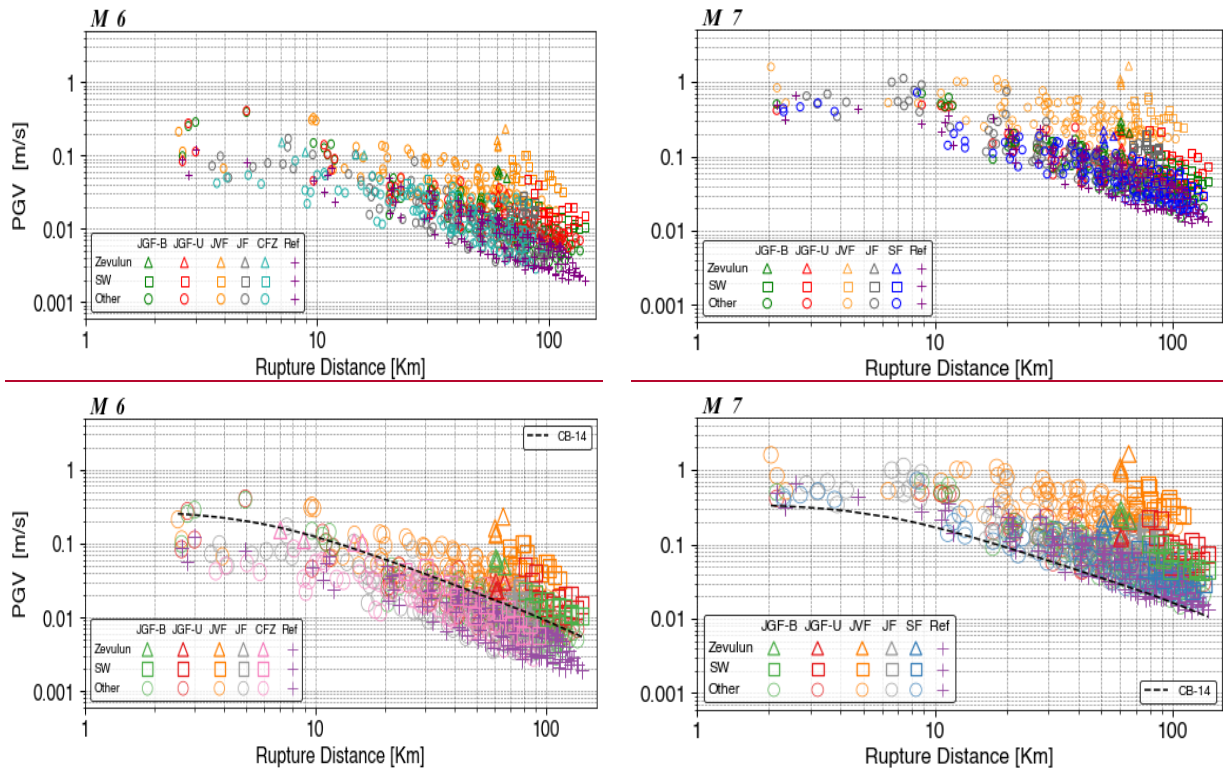
266 In this section, we report the simulation results and the simulation-based attenuation model for M 6 and M 7. We  
 267 begin with elaborating on the regression process and its deliverable, the attenuation model. Next, we show-present  
 268 the correspondence of the model with the simulated database in terms of PGV-ground motions variability, starting  
 269 from total and following with within-event, and between-event PGV residuals and examine the contribution of  
 270 each earthquake scenario to the total deviation. Then, we proceed with looking into single station variability,  
 271 through maps of the predicted and simulated PGV, with the corresponding residuals at each station. Finally, we



272 [examineshow](#) the PGV and the 5 %- 95 % ground motions significant duration ( $D_s$  595) correspondence between  
 273 predicted by global GMM's (CB14, Afshari & Stewart, 2016, respectively) and simulated.

#### 274 4.1 Simulation results

275 For each simulation, we attained a set of 129 synthetic ground motion records (3 components each: N-S, E-W,  
 276 and vertical) from the network deployed in the computational domain. Next, we calculated the PGV values for each  
 277 scenario at each station- as the maximum value over the three components. We decided to exclude some of  
 278 the M 7 near-source records (stations: 104,105 and 106 for the JVF scenario and stations: 122,123 and 129 for the  
 279 JGF-B, JGF-U, and Shemona scenarios) due to high strain values and possible non-linear effects, not compatible  
 280 with the linearity assumption of our model. In total, our ground motions database consists of 645 and 633 synthetic  
 281 records for M 6 and M 7, respectively. Figure 5 presents our results in terms of PGV as a function of distance. We  
 282 used different markers for records from the sedimentary structures of the Zevulun Valley and the Sedimentary  
 283 wedge to differentiate them from the remaining data.



284 **Figure 5.** Simulation results, PGV-distance space, for bilateral rupture on the Jordan Gorge Fault (JGF-B), Jericho Fault (JF)  
 285 Carmel Fault Zone (CFZ; for M 6) and the Shemona Fault (SF; for M 7), a southward unilateral rupture on the JGF (JGF-U),  
 286 and a super-shear rupture on the Jordan Valley Fault (JVF); for M 6 (left) and M 7 (right). The records from Zevulun Valley  
 287 and the Sedimentary wedge (SW) are marked with triangles and rectangles, respectively. The other records are marked with  
 288 circles; the reference records are marked with pluses. For comparison, the CB14 is plotted for a strike-slip fault,  $Z_{2.5}=0.42$   
 289 Km and  $V_{s30}=1686 \text{ m s}^{-1}$  (representing averaged values over all the sites).

#### 290 4.2 Statistical analysis of ground motions results

291 The next step was to formulate a statisticalparametric ground motion attenuation model (AM) for the two  
 292 magnitudes based on our simulations. Such a model will provide an estimate for the median ground motions and

293 their variability. The general parametric form of the AM for both M 6 and M 7 is based on the CB14 function and  
 294 presented in Eq. (1):

$$295 \ln Y = a \ln(\sqrt{R_{RUP}^2 + b}) + c \ln\left(\frac{V_{s,surf}}{V_{s,minref}} \frac{V_{s,surf}}{V_{s,ref}}\right) + d \frac{Z_2^2}{Z_2} + e \pm \sigma \quad (1)$$

296 Where Y is ground motion parameter-intensity measure (IM). Due to the bandwidth of our numerical models (0.1  
 297 to 1 Hz), we formulated the AM in terms of PGV. We used the closest distance to the fault rupture plane ( $R_{RUP}$   
 298 as defined in CB14) as the initial explanatory variable. To improve the accuracy of the model, we incorporated  
 299 two additional variables into the regressions: surface shear wave velocity at the site ( $V_{s,surf}$ ) and the depth to  $V_S$   
 300 = 2 km s<sup>-1</sup> ( $Z_2$ ), which is the depth to the hard Mesozoic sediments (top Judea Group-) considered the primary  
 301 reflector in the region.  $a$ ,  $b$ ,  $c$ ,  $d$ , and  $e$  are model coefficients, and  $\sigma$  is the standard deviation. The  $V_{s,minref}$  is the  
 302 minimum shear wave velocity corresponding to the Judea Group in the computational domain, which in our model  
 303 equals ~~6082000~~ 2000 m s<sup>-1</sup>.

304 The process of minimizing the residuals as a function of each explanatory variable can be found in the  
 305 supplementary material (Fig. S3). We used  $V_{s,surf}$  instead of the more common  $V_{S30}$ , as our grid resolution is 76  
 306 m, preventing us from accurately determining the time-averaged shear wave velocity in the top 30 m of each site  
 307 in our model. The coefficients and the total standard deviation for each model are summarized in Table 4.

308 **Table 4.** Regression coefficients for the attenuation model (AM)

Mag	IM	a	b	c	d		e		Standard Deviation ( $\sigma$ )
					<u><math>R_{rup} &gt; 58</math> km</u>	<u><math>R_{rup} &lt; 58</math> km</u>	<u><math>R_{rup} &gt; 58</math> km</u>	<u><math>R_{rup} &lt; 58</math> km</u>	
<u>Mag.</u>					<u>and <math>z_2 &gt; 0</math></u>	<u>or <math>z_2 = 0</math></u>	<u>and <math>z_2 &gt; 0</math></u>	<u>or <math>z_2 = 0</math></u>	
6	PGV	-1.01	59.34	-0.685	0		0.56		0.727 <u>6</u>
7	PGV	-1.422	<u>257.431</u> <u>51.81</u>	- 0.782 <u>669</u>	<u>-0.0256</u>	0	<u>42.08</u>	2.42	0.737629

### 309 4.3 AM Variability

310 ~~Following, we~~ We then examined the simulated data and the contribution of each scenario to the AM variability.  
 311 We calculated the within-event ( $\delta W$ ) and between-event ( $\delta B$ ) residuals (see Al Atik et al., (2010)) for each  
 312 magnitude and distance:

$$313 \delta W_{i,j} = \ln PGV_{i,j}^{sim} - \ln PGV_i^m \quad (2)$$

$$314 \delta B_i = \ln PGV_i^m - \ln PGV^{AM} \quad (3)$$

315 where  $PGV_{i,j}^{sim}$  is the simulation value for event  $i$  and recording  $j$ ,  $PGV_i^m$  is the median for event  $i$ , and  $PGV^{AM}$  is  
 316 the AM median value. The total residual is the sum of the within and between event residuals.

317 The residuals are presented in Fig. 6: total (Fig. 6a and 6b), within-event (Fig. 6c and 6d), and between-  
 318 events (Fig. 6e, and 6f). ~~The within event residuals (Fig. 6c,d) do not exhibit apparent bias or trend. However,~~  
 319 ~~some of the between event residuals (Fig. 6e,f) exhibit distance dependency. Most clearly, for M 7, the JVF~~  
 320 ~~(super shear model) and JGF U (directivity model) residuals increase with rupture distances greater than 30 km.~~  
 321 ~~The JVF residuals also demonstrate the same distance dependency for M 6; however, the effect is less prominent~~

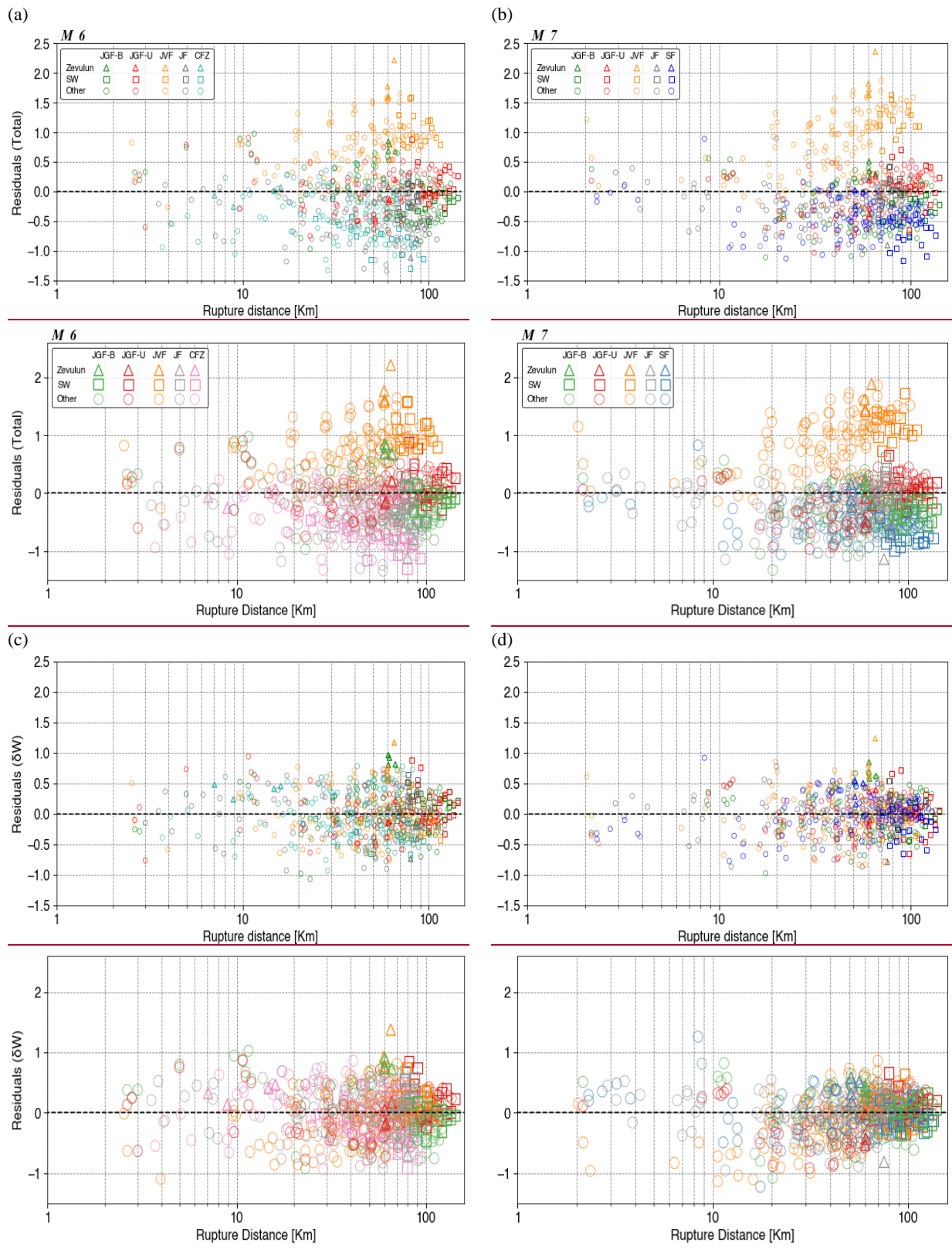
322 ~~when compared to M 7. The JGF-U does not exhibit an apparent trend for M 6.~~The total residuals (Fig. 6a and  
323 6b) show a large underprediction of the PGV from the JVF scenario (orange) on which we modeled a super-shear  
324 rupture, up to a ratio of ~~almost 2.5 and 2~~ in the Zevulun Valley (orange triangles), for ~~both magnitudes M 6 and M~~  
325 ~~7, respectively~~. However, the AM also exhibits over predictions; The PGV from the scenarios nucleated in the  
326 crystalline basement (SF, JF, and CFZ), with rupture speed= 3195 m s<sup>-1</sup>), are overpredicted down to a ratio of  
327 ~~almost -1.5, more than -1 (in ln units)~~.

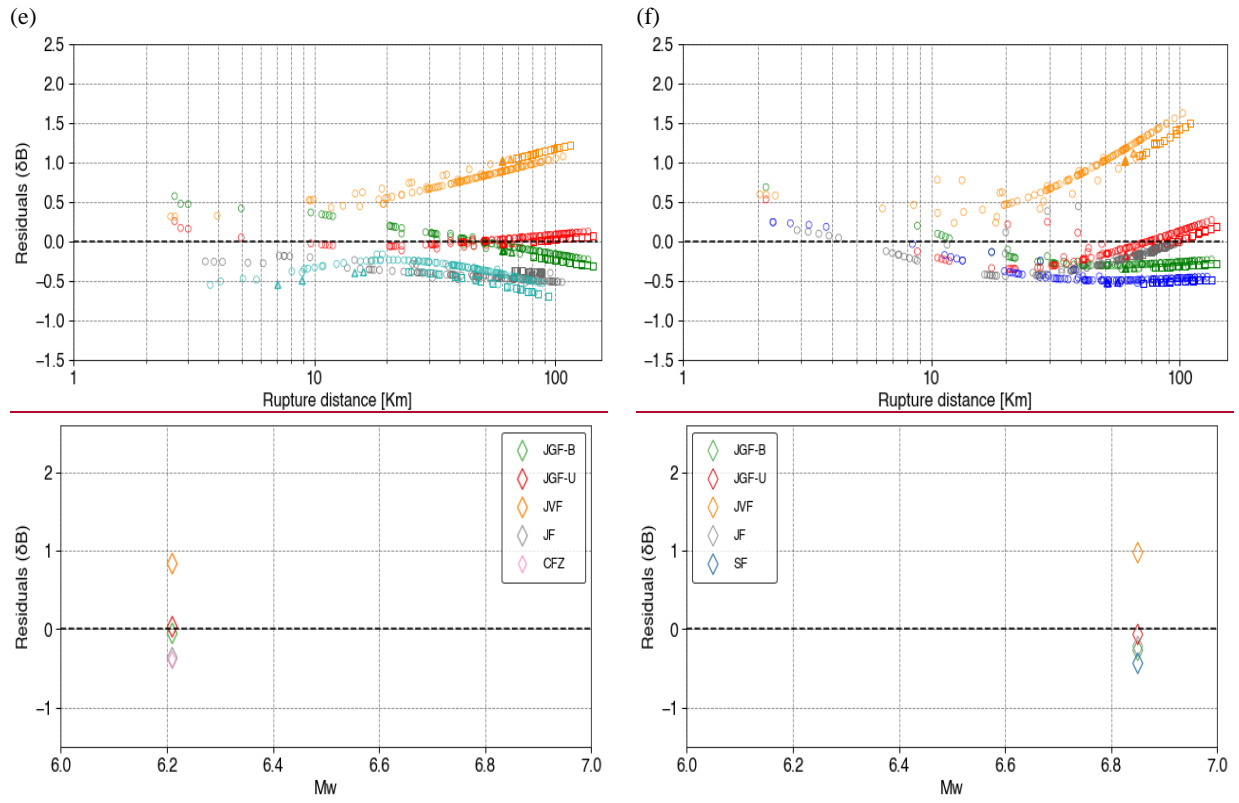
328 ~~For~~Some within-event residuals exhibit distance dependency; for M 7, the JVF (super-shear model) and  
329 ~~JGF scenarios, as shown in Fig 5, there is a tradeoff between~~U (directivity model) residuals increase with rupture  
330 ~~distances greater than 20 km. The JVF residuals also demonstrate the ground motion intensity in same distance~~  
331 ~~dependency for M 6; however, the effect is less prominent when compared to M7.~~

332 The effect of the rupture directivity (JGF-U) is demonstrated in comparing the Zevulun Valley (~~triangles~~)  
333 and the Sedimentary wedge (~~rectangles~~within-event residuals (Fig. 6c and 6d)). While in a symmetric rupture  
334 (JGF-B), the seismic energy dissipates equally into the north and south parts of the model, in an asymmetric  
335 rupture (JGF-U), more energy propagates toward the south, resulting in stronger ground motions at the  
336 Sedimentary wedge- (Fig. 5). However, the ground motions are less intensive at the Zevulun Valley compared to  
337 the symmetric rupture. As a result, the within-event residuals for Zevulun Valley are higher for the JGF-B scenario  
338 compared to the JGF-U scenario, while for the Sedimentary wedge, the opposite is true.

339  
340

Most clearly, the JVF between-event residuals are the highest for both M 6 and M 7 with a ratio of 1 (Fig. 6e, and 6f).





341 **Figure 6.** Residuals between simulated and attenuation model (AM) PGV as a function of rupture distance ( $R_{RUP}$ ), for bilateral  
 342 rupture on the Jordan Gorge Fault (JGF-B), Jericho Fault (JF) Carmel Fault Zone (CFZ; for M 6) and the Shemona Fault (SF;  
 343 for M 7), a southward unilateral rupture on the JGF (JGF-U), and a super-shear rupture on the Jordan Valley Fault (JVF); for  
 344 M 6 (left) and M 7 (right); (a) and (b) total residuals, (c) and (d) within-event ( $\delta W$ ) residuals, (e) and (f) between-event ( $\delta B$ )  
 345 residuals. The records from Zevulun Valley and the Sedimentary wedge (SW) are marked with triangles and rectangles,  
 346 respectively. The other records are marked with circles. Residuals are in ln units.

347 We further studied the single station variation of ground motions and quantified the misfit between the  
 348 simulated PGV and the AM PGV. We calculated the mean ground motion and its standard deviation at each  
 349 station. The residuals for single station  $k$  were calculated as follows:

$$350 \delta_k = \ln PGV_k^{sim} - \ln PGV_k^{AM} \quad (4)$$

351 where  $PGV_k^{sim}$  and  $PGV_k^{AM}$  are the simulated and predicted mean PGV at station  $k$ , respectively. Figure 7 and  
 352 Figure 8 show the mean simulated and mean AM PGVs for M 6 and M 7, respectively. For each station, we also  
 353 plotted the standard deviation using a scaled diameter circle.

354 Both figures show that simulated ground motions variability at a single station is large, not fully covered  
 355 by the AM. For example, simulated ground motions at station 129 (for location, please refer to Fig S1) located on  
 356 the Hula Valley exhibit a significant standard deviation. For M 6, it is the largest value (green triangle) of  $0.17 \text{ m s}^{-1}$   
 357 compared to  $0.09 \text{ m s}^{-1}$  (indigo) predicted by the AM, while for M 7, the largest standard deviation is  $0.59 \text{ m s}^{-1}$   
 358 (orange triangle) compared to  $0.02 \text{ m s}^{-1}$  (light green triangle) observed at station 127 located on the Zevulun  
 359 Valley (for location, please refer to Fig S1). As a result, there is a large discrepancy between the simulated and  
 360 AM values at specific stations.

361 **In general, higher mean PGV values are accompanied by a larger standard deviation for both magnitudes;**  
 362 **however, the ground motions variability is larger for M 7.**

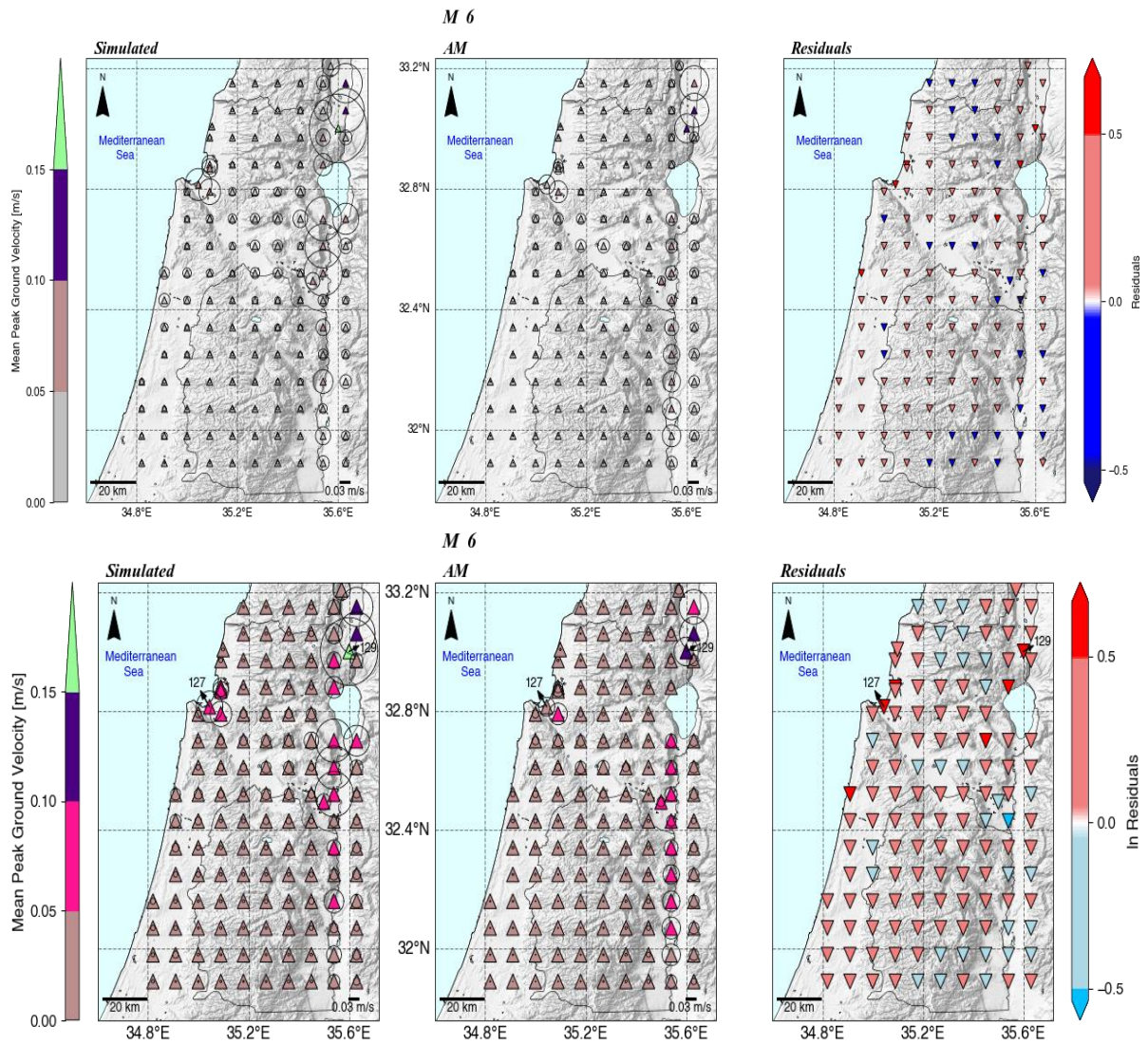


363 In general, as expected from normal log distribution, higher mean PGV values are accompanied by a  
364 larger standard deviation for both magnitudes. It is of significance for seismic hazard assessment, as outlier  
365 ground motions at specific sites, mainly from  $M < 7$  earthquakes, could be a significant source of damage  
366 (Minson et al., 2020)

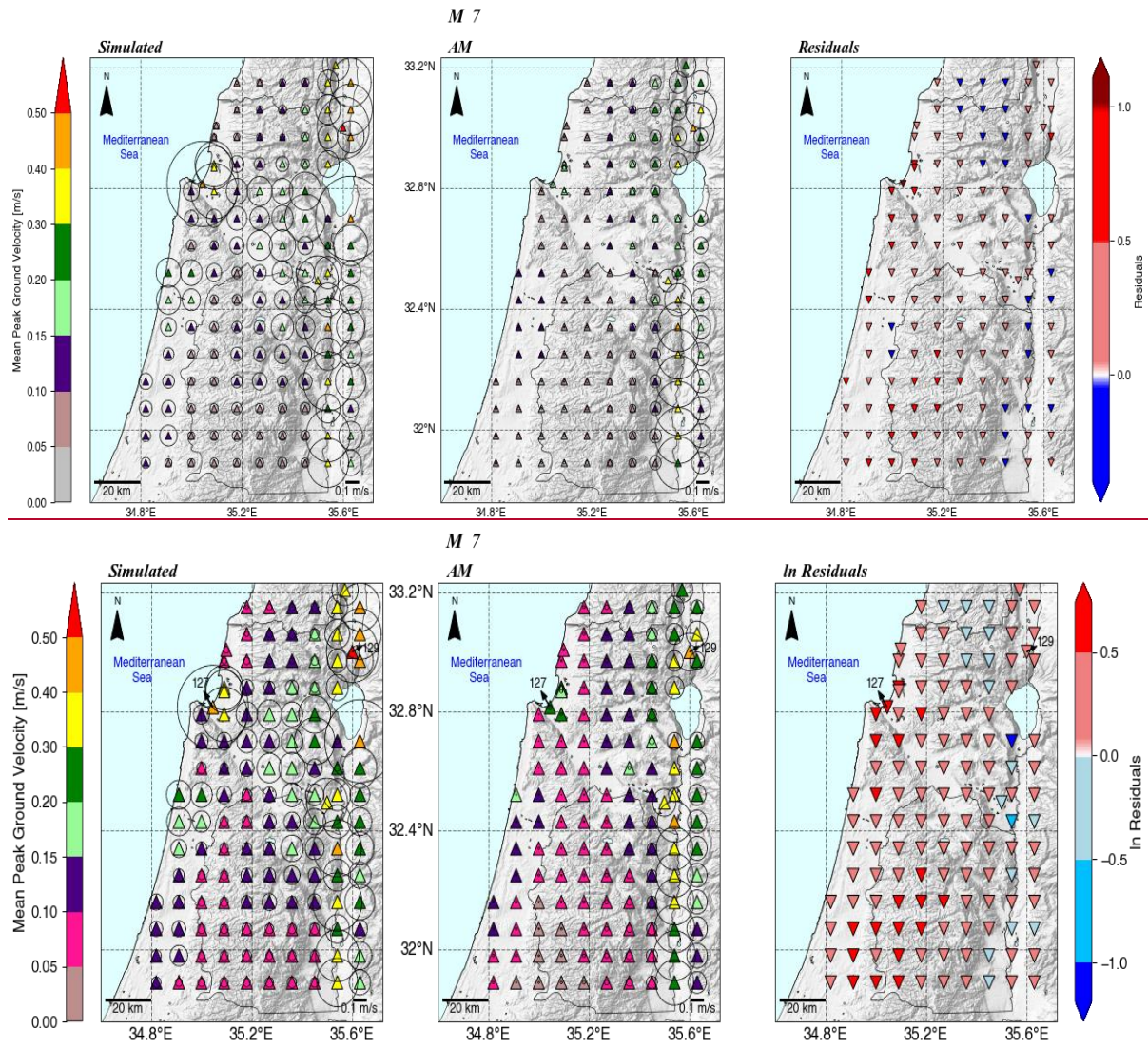
#### 367 4.4 Comparison with global models

368 To examine the agreement between our simulations with an instrumental, global GMM, we calculated the total  
369 residuals between PGVs from our simulations and PGVs predicted by the ~~CB-14 model~~. CB14 model. We chose  
370 the CB14 model as it is planned to supersede the CB08 model used in the Israel Building Code (413). The CB14  
371 PGVs were calculated for a strike-slip fault, where we used the surface shear wave velocity as the  $V_{s30}$  parameter  
372 and the basin response term  $Z_2$  as  $Z_{2.5}$ . Figure 9 shows the total residuals for the AM and CB14 models as a  
373 function of distance ( $R_{RUP}$ ). For both magnitudes, the AM (mean and standard deviation) oscillates near the zero-  
374 model bias (black horizontal dotted line). However, it deviates when approaching the region containing rupture  
375 distances typical of the Zevulun Valley. The effect is more noticeable for M 7. Figure 9 also shows that the CB14  
376 is less consistent and performs differently for each magnitude. While for M 6, the ~~GMPEGMM~~ mostly over  
377 predicts (negative values) the simulated PGV (until reaching ZV and SW rupture distances zones), for M 7, it  
378 mostly under predicts them (positive values), except for large distances, up to a factor of 2 and above. In addition,  
379 the ~~CB-14 exhibits~~ residuals calculated with respect to CB14 exhibit a significant standard deviation of the mean  
380 ground motion, with considerably larger variability for M 7.

381 It is important to note that, by averaging the PGVs, we subdue the performance of both models at individual  
382 stations/Rupture distances; thus, we cannot analyze the residual's spatial variations at a specific location.  
383 However, it is sufficient to demonstrate that the global model deviates considerably from simulated ground  
384 motions.

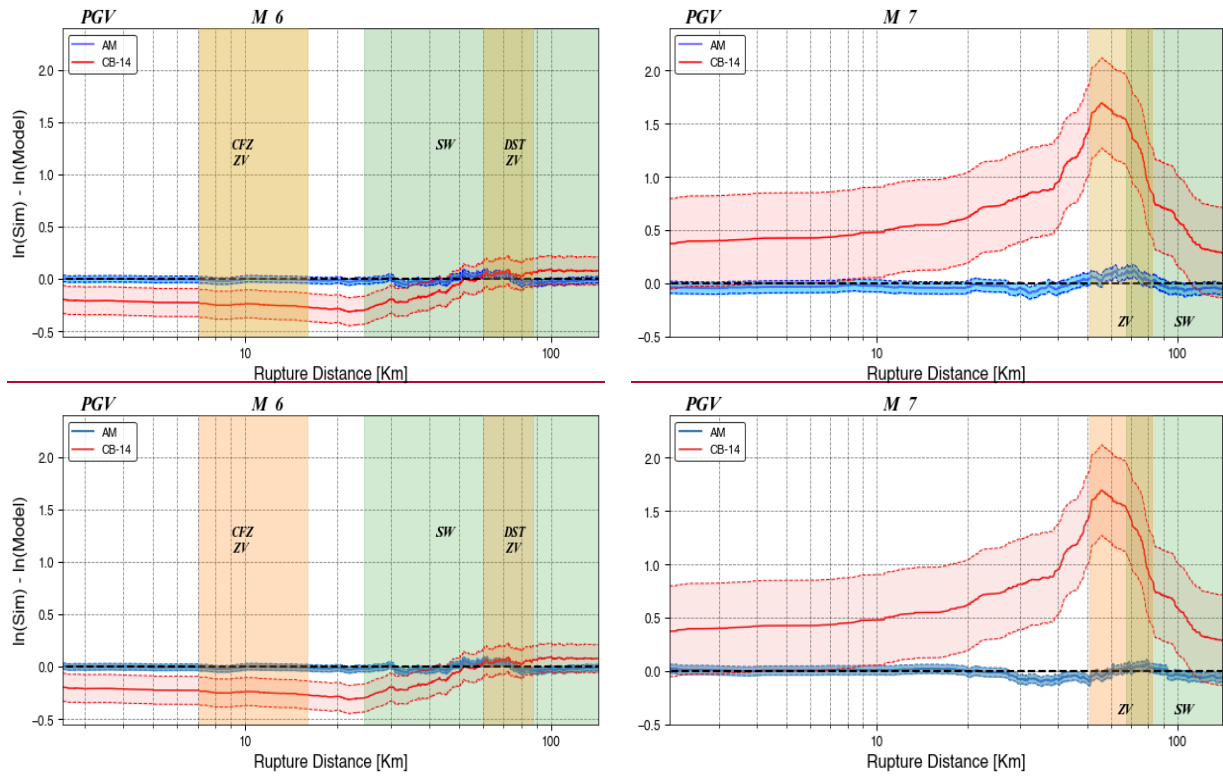


386 **Figure 7.** Map view of simulated and AM mean PGV (triangles) for M 6 and their standard deviation (diameter of the circles)  
 387 at each station, with the respective residuals in ln units (inverted triangles).



388 **Figure 8.** Map view of simulated and AM mean PGV (triangles) for M 7 and their standard deviation (diameters of the circles)  
 389 at each station, with the respective residuals in ln units (inverted triangles).





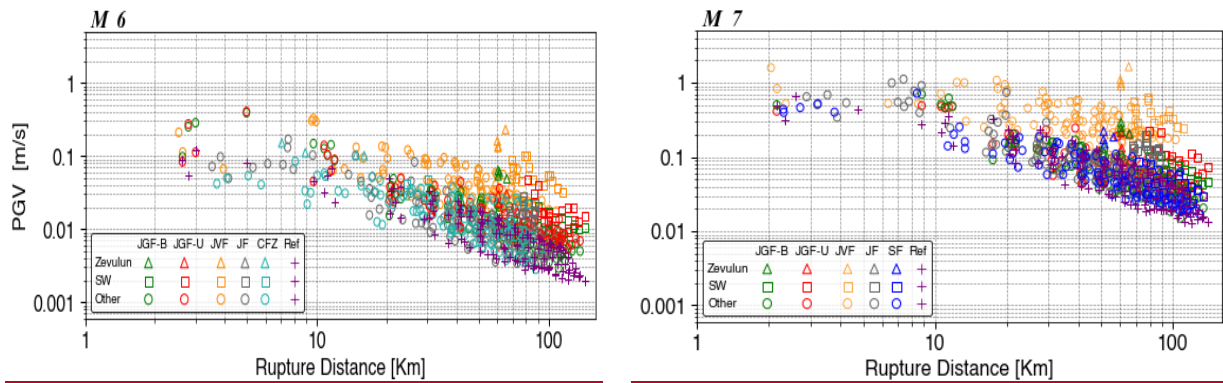
390 **Figure 9.** PGV Residuals between simulated (Sim) and predicted by the AM (blue) and ~~CB-14~~CB14 (red) models, as a function  
 391 of rupture distance ( $R_{RUP}$ ), for M 6 (left) and M 7 (right). Thick lines represent the mean, and the shaded region denotes the  
 392 standard deviation at each distance. The green and yellow shaded regions indicate the range of rupture distances related to the  
 393 Sedimentary wedge (SW) and the Zevulun Valley (ZV), respectively. Residuals are in ln units.

#### 394 4.5 Significant duration

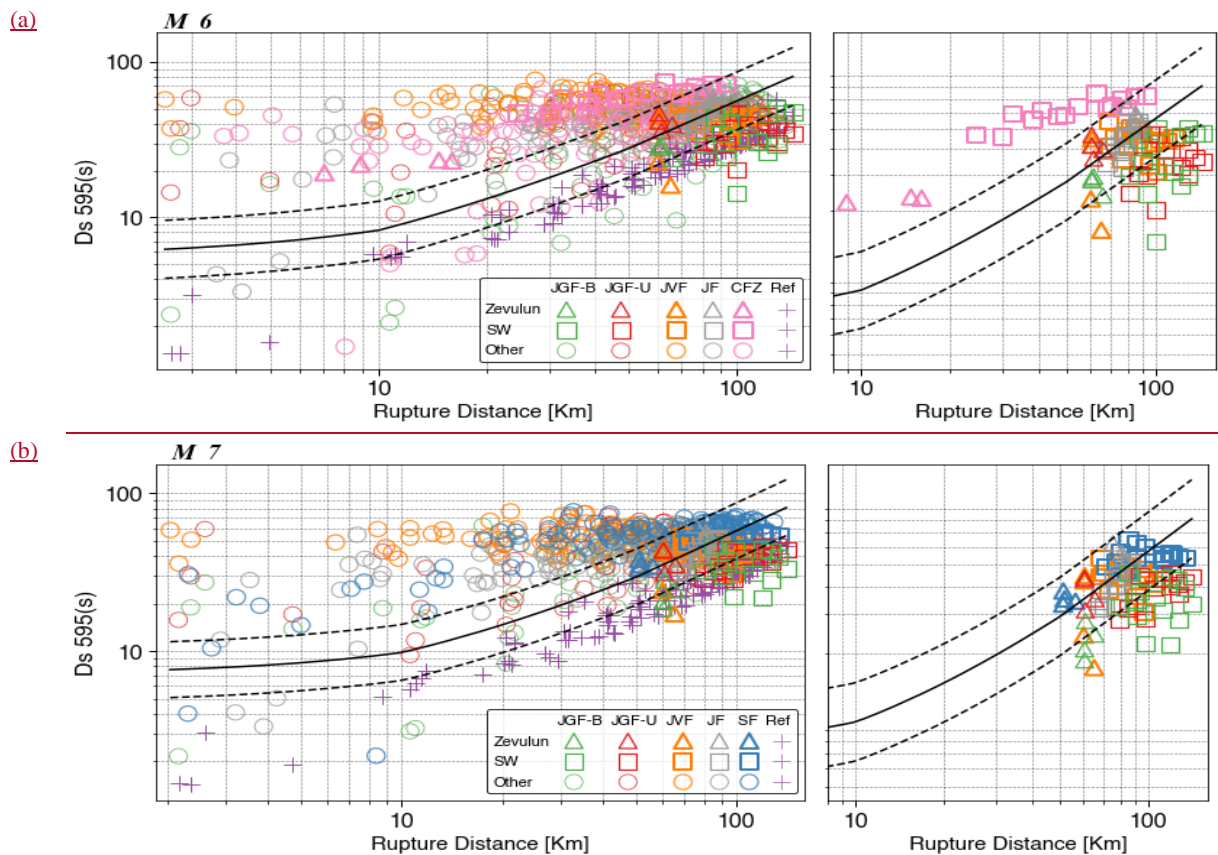
395 Another important intensity measure is the significant duration ( $Ds_{595}$ ), the time interval between 5 % to 95 %  
 396 of the cumulative seismic energy (Arias Intensity) at a site. Figure 10 shows the simulated and empirical  $Ds_{595}$   
 397 values as a function of rupture distance. The typical increase of the empirical model with distance is captured in  
 398 the reference (laterally homogenous) model. However, for all other models, the significant duration remains nearly  
 399 constant, at ruptures distances larger than 20 km. In addition, the empirical GMM mostly under-predicts the  
 400 simulated values between 2 to 50 Km for both magnitudes.

401 We postulate that this is caused by the complex geological setting of our model. The impact of geological  
 402 complexity is reflected in  $Ds_{595}$  values from ~~Zevulun Valley (triangles) and the Sedimentary wedge (rectangles).~~  
 403 ~~The energy accumulates faster in these near near-source stations, Zevulun Valley (triangles), and the Sedimentary~~  
 404 ~~wedge (rectangles). At near-source stations, the significant duration is large due to the effects of deep sedimentary~~  
 405 ~~structures along the DST, which also prolongs the path duration of the ground motions in other sites (Shimony et~~  
 406 ~~al., 2021), resulting in long significant duration with almost no path dependency. On the contrary at the Zevulun~~  
 407 ~~Valley and the SW, the energy accumulates faster~~ than in other sites, as the ground motions are amplified, reaching  
 408 95 % of the total energy over a shorter duration. Interestingly, the significant duration in Zevulun Valley is lower  
 409 than in the Sedimentary wedge. As we expect from deep sedimentary structures to prolong shaking duration, it  
 410 may sound counterintuitive. However, it is explained by the relative proximity of the Zevulun Valley to the  
 411 rupture. Whereas in Zevulun Valley, most of the energy arrives as a pulse at the beginning of the record, the

412 energy at the more distant Sedimentary wedge accumulates more gradually and reaches its maximum almost at  
 413 the end of the record, resulting in higher/longer  $D_s$  595 values. In general, there is no large deviation between the  
 414 simulated significant duration for M 6 and M 7. However, the empirical model shows a longer duration for M 7.  
 415 This resembles in source duration is related to the DSM settings, more specifically to the source fundamental  
 416 frequency, which in our study, is the same for both magnitudes; and it is a subject for testing in future works.



417



418 **Figure 10.** Comparison of 5 % to 95 % ground motions significant duration ( $D_s$  595) comparison between simulated and  
 419 empirical GMM (Afshari & Stewart, 2016), for bilateral rupture on the Jordan Gorge Fault (JGF-B), Jericho Fault (JF) Carmel  
 420 Fault Zone (CFZ; for M 6) and the Shemona Fault (SF; for M 7), a southward unilateral rupture on the JGF (JGF-U), and a  
 421 super-shear rupture on the Jordan Valley Fault (JVF); for M 6 (a) and M 7 (b). Main plots (left) accompanied with subplots  
 422 showing only the records from the Zevulun Valley and the Sedimentary wedge (right). Solid and dashed lines represent the  
 423 median and the standard deviation of the empirical GMM, respectively for M 6 (left) and M 7 (right). Solid and dashed lines



424 ~~represent the median and the standard deviation of the empirical GMM, respectively.~~ The records from Zevulun Valley and  
425 the Sedimentary wedge (SW) are marked with triangles and rectangles, respectively. The other records are marked with circles.

## 426 5 Discussion and Summary

427 A strong earthquake in Israel is imminent. However, up to date, a comprehensive regional GMM describing the  
428 spatial variability of ground motions has not yet been developed. This is mainly due to low seismicity rates and  
429 magnitude bounded strong motion database, coupled with sparse instrumental coverage. The current ground  
430 motion database lacks events with magnitude  $M > 6$ . To ~~fill this gap and~~ examine different source and path effects  
431 on ground motions variability, we simulated M 6 and M 7 earthquakes with different source and path properties.  
432 Subsequently, to study the ground motions variability, we developed a ~~statistical parametric~~ attenuation model  
433 (AM) of PGV for M 6 and M 7 earthquakes, based on  $R_{RUP}$ ,  $Z_2$ , and  $V_{S, surf}$  explanatory values.

434 Our analysis showeds that the AM was unable to fully capture the variability of the simulated ground  
435 motions. Except for the Jordan Valley Fault (JVF) scenarios, the AM overestimates most of the modeled ground  
436 motions. We postulate that this overestimation results from the outlier, higher PGV values from the JVF scenario  
437 (Fig. 5), shifting the average ground motion toward them. Also, the within-event residuals for the JVF scenario  
438 show a distance dependency for  $R_{RUP} > 20$  Km, continuing to grow away from the fault. We describe this scenario  
439 as a "black swan" of our simulations and account its outlier behavior to the effects of the super-shear rupture,  
440 specific to this model,  affecting both the source (between-event residuals) and path (within-event residuals) terms  
441 of the ground motions (Fig.6). Super-shear ruptures behave differently from sub-shear ruptures in many aspects.  
442 Most pertinent to our analysis is the slow energy decay of the super-shears relative to sub-shears (Bhat et al.,  
443 2007); thus, it cannot be fully captured by our AM, which is based mainly on sub-shear ruptures. In addition, it  
444 was found that  $Z_2$  depth to Mesozoic rock,  is not a good predictor for has a very small impact ( $<0.001$ ) on the  
445 standard deviation for the M 6, reducing it from 0.5998 to 0.5988 (Fig. S3). As a result, the M 6 model depends  
446 only on rupture distance and  $V_{S, surf}$ . For M 7,  $Z_2$  is a good predictor for soil sites ( $Z_2 > 0$ ) located  $>58$  Km from the  
447 source, including the Zevulun Valley and the Sedimentary wedge (Fig. 6d), imposing a great seismic hazard. We  
448 do not see a clear dependence of the deep sedimentary structures with  $Z_2$  along the DST. We speculate that Their  
449 site response may be masked by nearby source effects and requires additional analysis.

450 For each scenario, both magnitudes considered, we observed high PGV values at the Zevulun Valley and  
451 the Sedimentary wedge associated with local site effects. These sedimentary structures exhibit a larger  
452 discrepancy between the simulated and AM PGV values when compared with other sites. Such deviation indicates  
453 that the AM does not fully capture the site effects of these complex structures, and future model refinements are  
454 required. Likewise, the single station variability shows that the simulated values' highest mean and standard  
455 deviation were in Zevulun Valley and near-source stations. In addition, a relatively high standard deviation was  
456 also found in the Sedimentary wedge for M 7. This large single station variability is, apparently, the impact of the  
457 outlier JVF PGV values. The AM does not account for the standard deviation at near-source and Zevulun Valley  
458 stations for the M 6 and almost at all stations for the M 7. In fact, as the AM was unable to capture the simulated  
459 JVF PGV values, it is expected that the single station variability cannot be captured either. Furthermore, ~~we show~~  
460 ~~that~~ the larger discrepancy for M 7 is due to the larger deviation of the JVFs ground motions from those of sub-  
461 shear ruptures (Fig. 5), on which the AM is mainly based. the mean (Fig. 6d,e).

462 Noteworthy to mention is that while the effect of the super-shear rupture on the AM performance is  
463 systematic over the entire computational domain, comprised of both source and path effects (Fig. 6), the effect of  
464 the southward directivity is distance-dependent, path effect, increasing towards the south, related to a larger  
465 amount of energy discharged in this direction. Additional records of super-shear and directivity ruptures and  
466 accounting for these source effects by additional model terms will improve the performance of the AM and will  
467 assist in better understanding the implications of these phenomena on the seismic hazard in Israel.

468 The comparison of the simulated ground motions with a global GMM ~~model (CB-14)~~(CB14) showed that  
469 this model is not well constrained for the simulated ground motions and does not capture their total variability.  
470 We note that the comparison was performed on a single IM, the PGV values, one of several intensity measures  
471 provided by the ~~CB-14~~CB14. Thus, our findings are pertinent to the variability of PGV solely. It should be noted  
472 that PGV is a good proxy for structural damage (e.g., to Kaestli & Fäh, (2006); Wald et al., (1999)Kaestli & Fäh,  
473 (2006); Wald et al., (1999)), hence a crucial parameter for seismic hazard mitigation. This discrepancy between  
474 modeled PGV and ~~CB-14~~CB14 PGVs, will inevitably result in a discrepancy in the evaluation of structural  
475 damage.

476 The significant duration ( $D_{s595}$ ) comparison showed again that the imported model performs differently  
477 than the simulated ground motion and cannot explain the local variability due to complex geological structure,  
478 affecting the source ~~path and site terms of the ground motions~~, path, and site terms of the ground motions, such  
479 as the path independence of the significant duration. However, we note that the  $D_{s595}$  from our simulations were  
480 calculated based on low frequency content (<1Hz) and may be biased from  $D_{s595}$  calculated based on the  
481 complete spectrum comprised of both low and high frequencies. The effects of the frequency content on significant  
482 duration may be a potential topic for research in future works.

483 Regional simulations of near-fault ground motions from large Mw 7 earthquakes in Lebanon, based on a  
484 1-D velocity approximation, were presented by Fayjaloun et al., (2021). A comparison between the results  
485 reported by Fayjaloun et al., (2021) with our results is somewhat limited. Specifically, it was shown that structural  
486 and material heterogeneity of the crust in Israel results in regional ground motions variability (Volk et al., 2017;  
487 Shani-Kadmiel et al., 2020; Shimony et al., 2021). These effects could only be captured by 3-D modeling.

488 We acknowledge that our AM is not independent of the evaluated models, thus describing both their  
489 explanatory and predictive power (Mak et al., 2017). However, our goal was not to develop an independent and  
490 comprehensive GMM but to study the ground motion variability through a ~~statistical ground motion~~parametric  
491 model.

492 Recently, Maiti et al., (2021) developed a suite of nine GMMs for Israel, in the magnitude range of 3 to 8  
493 and distance range of 1 to 300 Km. These models are formulated in Fourier amplitude spectra (FAS) and are based  
494 on one empirical and four simulated ground ~~motions~~motion datasets and two empirical host models. The simulated  
495 ground motions were generated using the Stochastic Method SIMulation (SMSIM) model of Boore (2003), with  
496 a unique set of parameters for each simulation, calibrated with the empirical ground motions dataset (discussed in  
497 detail in Yagoda-Biran et al., (2021)). However, the GMMs do not fully account for a local source, path, and site  
498 effects due to sparse empirical database at large magnitudes ( $M > 6$ ) and the utilization of a point-source stochastic  
499 simulation method. This method is useful for simulating mean ground motions. Yet, it is less appropriate for  
500 simulating site-specific and earthquake-specific ground motions and low-frequency ground motions, which are  
501 affected by the 3D geometry of the computational domain. The AM presented in this work is based on 3D

502 simulations and incorporates a finite fault source with different rupture properties. This is the first step toward  
503 developing a regional GMM, accounting for local source, path, and site effects. In subsequent work, which is  
504 beyond the scope of the current research, we intend to develop a complete GMM for Israel, which will include all  
505 the magnitudes and will be based on empirical ( $M < 6$ ) as well as on synthetic ( $M > 6$ ) databases. In addition, we  
506 plan to incorporate new path and site terms such as  $Z_{0.8}$  for the Zevulun valley and the Sedimentary wedge,  
507 distance-dependent and rupture velocity-dependent attenuation for Directivity and super-shear ruptures, among  
508 others; as well as a source term for super-shear ruptures. Such a model is expected to perform better than imported  
509 global models by maintaining both; a lower aleatory variability and, as new synthetic data will be added to the  
510 database, reduced epistemic uncertainty of the median ground motions (Abrahamson et al., 2019).

511 ~~To summarize, the~~The population of Israel is fast-growing, with an annual rate of 1.8 % (OECD 2020  
512 data), compared with the 0.4 % average of the OECD. Coupled with fast economic growth of 4.5 % (OECD 2019  
513 data), the demand for housing and infrastructure constantly elevates the seismic risk in Israel. Our work shows  
514 that the ground motions in Israel from M 6 and M 7 earthquakes are expected to be very damaging, up to 8-9 EMS  
515 (Fig. S4). Furthermore, the modeled ground motions exhibit considerable spatial variability, which imported  
516 GMMs do not fully capture. The development of a local comprehensive GMM model is therefore critical for the  
517 mitigation of seismic risk. In the foreseen future, the moderate-strong ground motion data gap will be filled by  
518 synthetic ground motion records from systematic numerical simulations.

## 519 **Data and resources**

520 Israel Seismic catalog (Fig. 1a), expanded after Wetzler & Kurzon (2016) catalog and the configuration of the  
521 Israel seismic network (Fig. 1b) after Kurzon et al., (2020) can be found at  
522 <https://earthquake.co.il/en/earthquake/searchEQS.php> and <https://earthquake.co.il/en/network/accNetwork.php>,  
523 respectively. The ground motions database of Israel (Fig. 2) discussed in Yagoda-Biran et al., (2021) is available  
524 at <https://earthquake.co.il/en/hazards/EngSeismology.php>. The Taub Center population projections for Israel are  
525 accessible at <https://www.taubcenter.org.il/en/pr/population-projections-for-israel-2017-2040/>. OECD population  
526 and economic growth rates can be found at <https://data.oecd.org/israel.htm#profile-economy>. Simulations were  
527 performed using SW4 version 2.0 (v2.0; Petersson and Sjögreen, 2017a), an open-source package for wave  
528 propagation simulations, available at [github.com/geodynamics/sw4](https://github.com/geodynamics/sw4) (last accessed June 2021). Data processing  
529 was done with the pySW4 package from Shahr Shani-Kadmiel, available at  
530 <https://github.com/shaharkadmiel/pySW4> (last accessed July 2021), and "obsPy" (Beyreuther et al., 2010),  
531 developed for numerical seismology. Figures were prepared with Matplotlib (Hunter, 2007) and Cartopy (Met  
532 Office, 2016). Peak ground velocity (PGV) values, according to Campbell and Bozorgnia (2014), were calculated  
533 using the Next Generation Attenuation-West Project (NGA-West2) ground-motion prediction equations (GMPEs)  
534 excel file, available at <https://apps.peer.berkeley.edu/ngawest2/databases/> (last accessed July 2021). The  
535 supplemental material includes: (1) synthetic station network deployed in our models (Fig. S1); (2) distributed  
536 slip model (DSM) slip distribution and rupture time (Fig. S2); (3) the evolution of the residuals between simulated  
537 and attenuation model (AM) PGV for M 6 and M 7 (Fig. S3) and (4) map view of simulated mean EMS intensity  
538 calculated according to Kaestli & Fäh, (2006).

539 *Competing interests.* The authors declare that they have no conflict of interest.

540 **Acknowledgments**

541 This research was partially funded by the Ministry of Energy, Israel (Grant Number 219-17-02). Co-author JG  
542 was partially supported by the Ministry of Energy scholarship for graduate studies (Tender 76/19).

543 **References**

- 544 Abrahamson, N. A., Kuehn, N. M., Walling, M., and Landwehr, N.: Probabilistic seismic hazard analysis in  
545 California using nonergodic ground-motion models, *Bull. Seismol. Soc. Am.*, 109, 1235–1249,  
546 <https://doi.org/10.1785/0120190030>, 2019.
- 547 Afshari, K. and Stewart, J. P.: Physically parameterized prediction equations for significant duration in active  
548 crustal regions, *Earthq. Spectra*, 32, 2057–2081, <https://doi.org/10.1193/063015EQS106M>, 2016.
- 549 Agnon, A.: Pre-instrumental earthquakes along the Dead Sea rift, in: *Modern Approaches in Solid Earth*  
550 *Sciences*, vol. 6, Springer, 207–261, [https://doi.org/10.1007/978-94-017-8872-4\\_8](https://doi.org/10.1007/978-94-017-8872-4_8), 2014.
- 551 Aldersons, F., Ben-Avraham, Z., Hofstetter, A., Kissling, E., and Al-Yazjeen, T.: Lower-crustal strength under  
552 the Dead Sea basin from local earthquake data and rheological modeling, *Earth Planet. Sci. Lett.*, 214, 129–142,  
553 [https://doi.org/10.1016/S0012-821X\(03\)00381-9](https://doi.org/10.1016/S0012-821X(03)00381-9), 2003.
- 554 Ambraseys, N. N.: Comparison of frequency of occurrence of earthquakes with slip rates from long-term  
555 seismicity data: The cases of Gulf of Corinth, Sea of Marmara and Dead Sea Fault Zone, *Geophys. J. Int.*, 165,  
556 516–526, <https://doi.org/10.1111/j.1365-246X.2006.02858.x>, 2006.
- 557 Anderson, J. G. and Brune, J. N.: Probabilistic seismic hazard analysis without the ergodic assumption, *Seismol.*  
558 *Res. Lett.*, 70, 19–28, <https://doi.org/10.1785/gssrl.70.1.19>, 1999.
- 559 Al Atik, L., Abrahamson, N., Bommer, J. J., Scherbaum, F., Cotton, F., and Kuehn, N.: The variability of  
560 ground-motion prediction models and its components, *Seismol. Res. Lett.*, 81, 794–801,  
561 <https://doi.org/10.1785/gssrl.81.5.794>, 2010.
- 562 Bartov, Y., Steinitz, G., Eyal, M., and Eyal, Y.: Sinistral movement along the Gulf of Aqaba - Its age and  
563 relation to the opening of the Red Sea, *Nature*, 285, 220–222, <https://doi.org/10.1038/285220a0>, 1980.
- 564 Ben-Avraham, Z., Ginzburg, A., Makris, J., and Eppelbaum, L.: Crustal structure of the Levant Basin, eastern  
565 Mediterranean, 346, 23–43, [https://doi.org/10.1016/S0040-1951\(01\)00226-8](https://doi.org/10.1016/S0040-1951(01)00226-8), 2002.
- 566 Beyreuther, M., Barsch, R., Krischer, L., Megies, T., Behr, Y., and Wassermann, J.: ObsPy: A python toolbox  
567 for seismology, *Seismol. Res. Lett.*, 81, 530–533, <https://doi.org/10.1785/gssrl.81.3.530>, 2010.
- 568 Bhat, H. S., Dmowska, R., King, G. C. P., Klinger, Y., and Rice, J. R.: Off-fault damage patterns due to  
569 supershear ruptures with application to the 2001 Mw 8.1 Kokoxili (Kunlun) Tibet earthquake, *J. Geophys. Res.*  
570 *Solid Earth*, 112, 1–19, <https://doi.org/10.1029/2006JB004425>, 2007.
- 571 Boore, D. M.: Simulation of ground motion using the stochastic method, *Pure Appl. Geophys.*, 160, 635–676,  
572 <https://doi.org/10.1007/PL00012553>, 2003.
- 573 Brocher, T. M.: Key elements of regional seismic velocity models for long period ground motion simulations, *J.*  
574 *Seismol.*, 12, 217–221, <https://doi.org/10.1007/s10950-007-9061-3>, 2008.
- 575 Campbell, K. W. and Bozorgnia, Y.: NGA ground motion model for the geometric mean horizontal component  
576 of PGA, PGV, PGD and 5% damped linear elastic response spectra for periods ranging from 0.01 to 10 s,  
577 *Earthq. Spectra*, 24, 139–171, <https://doi.org/10.1193/1.2857546>, 2008.
- 578 Campbell, K. W. and Bozorgnia, Y.: NGA-West2 ground motion model for the average horizontal components

579 of PGA, PGV, and 5% damped linear acceleration response spectra, *Earthq. Spectra*, 30, 1087–1114,  
580 <https://doi.org/10.1193/062913EQS175M>, 2014.

581 Chaljub, E., Moczo, P., Tsuno, S., Bard, P. Y., Kristek, J., Käser, M., Stupazzini, M., and Kristekova, M.:  
582 Quantitative comparison of four numerical predictions of 3D ground motion in the Grenoble Valley, France,  
583 *Bull. Seismol. Soc. Am.*, 100, 1427–1455, <https://doi.org/10.1785/0120090052>, 2010.

584 Douglas, J. and Aochi, H.: A survey of techniques for predicting earthquake ground motions for engineering  
585 purposes, *Surv. Geophys.*, 29, 187–220, <https://doi.org/10.1007/s10712-008-9046-y>, 2008.

586 Fayjaloun, R., Dabaghi, M., Cornou, C., Causse, M., Lu, Y., Stehly, L., Voisin, C., and Mariscal, A.: Hybrid  
587 Simulation of Near-Fault Ground Motion for a Potential Mw 7 Earthquake in Lebanon, *Bull. Seismol. Soc. Am.*,  
588 111, 2441–2462, <https://doi.org/10.1785/0120210091>, 2021.

589 Garfunkel, Z.: Lateral motion and deformation along the Dead Sea transform, in: *Modern Approaches in Solid*  
590 *Earth Sciences*, vol. 6, Springer International Publishing, 109–150, [https://doi.org/10.1007/978-94-017-8872-](https://doi.org/10.1007/978-94-017-8872-4_5)  
591 [4\\_5](https://doi.org/10.1007/978-94-017-8872-4_5), 2014.

592 Graves, R. and Pitarka, A.: Refinements to the Graves and Pitarka (2010) broadband ground-motion simulation  
593 method, *Seismol. Res. Lett.*, 86, 75–80, <https://doi.org/10.1785/0220140101>, 2015.

594 Graves, R., Jordan, T. H., Callaghan, S., Deelman, E., Field, E., Juve, G., Kesselman, C., Maechling, P., Mehta,  
595 G., Milner, K., Okaya, D., Small, P., and Vahi, K.: CyberShake: A Physics-Based Seismic Hazard Model for  
596 Southern California, *Pure Appl. Geophys.*, 168, 367–381, <https://doi.org/10.1007/s00024-010-0161-6>, 2011.

597 Grünthal, G., Hakimhashemi, A., Schelle, H., Bosse, C., and Wahlström, R.: The long-term temporal behaviour  
598 of the seismicity of the Dead Sea Fault Zone and its implication for time-dependent seismic hazard assessments,  
599 <https://doi.org/10.2312/GFZ.b103-09098>, 2009.

600 Gvirtzman, Z., Zilberman, E., and Folkman, Y.: Reactivation of the Levant passive margin during the late  
601 Tertiary and formation of the Jaffa Basin offshore central Israel, *J. Geol. Soc. London.*, 165, 563–578,  
602 <https://doi.org/10.1144/0016-76492006-200>, 2008.

603 Gvirtzman Z., I. M. and Sagee, Y.: Re-processing and geological re-interpretation of old seismic lines of Haifa  
604 bay, *Geol. Surv. Isr. GSI/27/2011*, 2011.

605 Gvitzman, Z. and Zaslavsky, Y.: Map of Zones with Potentially High Ground Motion Amplification:  
606 Explanatory Notes, Rep. Num. GSI/15/2009, 2009.

607 Hamiel, Y., Amit, R., Begin, Z. B., Marco, S., Katz, O., Salamon, A., Zilberman, E., and Porat, N.: The  
608 seismicity along the dead sea fault during the last 60,000 years, *Bull. Seismol. Soc. Am.*, 99, 2020–2026,  
609 <https://doi.org/10.1785/0120080218>, 2009.

610 Hamiel, Y., Piatibratova, O., and Mizrahi, Y.: Creep along the northern Jordan Valley section of the Dead Sea  
611 Fault, *Geophys. Res. Lett.*, 43, 2494–2501, <https://doi.org/10.1002/2016GL067913>, 2016.

612 Hunter, J. D.: Matplotlib: A 2D graphics environment, *Comput. Sci. Eng.*, 9, 90–95,  
613 <https://doi.org/10.1109/MCSE.2007.55>, 2007.

614 Israel Standards Institution: Standard SI 413. Design Provisions for Earthquake Resistance of Structures.  
615 Amendment No. 5, 2013.

616 Kaestli, P. and Fäh, D.: Rapid estimation of macroseismic effects and Shakemaps using macroseismic data, in:  
617 *1st European Conf. Earthquake Engineering and Seismology*, 1535, 2006.

618 Kuehn, N. M., Abrahamson, N. A., and Walling, M. A.: Incorporating nonergodic path effects into the NGA-



619 west2 ground-motion prediction equations, *Bull. Seismol. Soc. Am.*, 109, 575–585,  
620 <https://doi.org/10.1785/0120180260>, 2019.

621 Kurzon, I., Nof, R. N., Laporte, M., Lutzky, H., Polozov, A., Zakosky, D., Shulman, H., Goldenberg, A.,  
622 Tatham, B., and Hamiel, Y.: The “TRUAA” seismic network: Upgrading the Israel Seismic Network-toward  
623 national earthquake early warning system, *Seismol. Res. Lett.*, 91, 3236–3255,  
624 <https://doi.org/10.1785/0220200169>, 2020.

625 Lan, X., Xing, H., Zhou, J., and Zhao, J. X.: A comparison of the source, path, and site effects of the strong-  
626 motion records from the western and the southwestern parts of China with modern ground-motion prediction  
627 equations, *Bull. Seismol. Soc. Am.*, 109, 2691–2709, <https://doi.org/10.1785/0120180293>, 2019.

628 Maiti, S. K., Yagoda-Biran, G., and Kamai, R.: A Suite of Alternative Ground-Motion Models (GMMs) for  
629 Israel, *Bull. Seismol. Soc. Am.*, 111, 2177–2194, <https://doi.org/10.1785/0120210003>, 2021.

630 Mak, S., Cotton, F., and Schorlemmer, D.: Measuring the performance of ground-motion models: The  
631 importance of being independent, <https://doi.org/10.1785/0220170097>, 2017.

632 Met Office: Cartopy: a cartographic python library with a matplotlib interface, <http://scitools.org.uk/cartopy>,  
633 2016.

634 Minson, S. E., Baltay, A. S., Cochran, E. S., McBride, S. K., and Milner, K. R.: Shaking is almost always a  
635 surprise: The earthquakes that produce significant ground motion, *Seismol. Res. Lett.*, 92, 460–468,  
636 <https://doi.org/10.1785/0220200165>, 2020.

637 Mizutori, M. and D’ebarati, G.: The human cost of disasters: an overview of the last 20 years (2000-2019), UN  
638 Off. Disaster Risk Reduction., <https://doi.org/10.18356/79b92774-en>, 2020.

639 Pesaresi, M., Ehrlich, D., Kemper, T., Siragusa, A., Florczyk, A., Freire, S., and Corbane, C.: Atlas of the  
640 Human Planet 2017. Global Exposure to Natural Hazards. EUR 28556 EN, 92 pp., 2017.

641 Petersson, N. A. and Sjogreen, B.: SW4 Users Guide, Lawrence Livermore Natl. Lab. Tech. Rep. LLNL-SM,  
642 662014, 2014.

643 Petersson, N. A. and Sjogreen, B.: SW4, version 2.0, Computational Infrastructure of Geodynamics,  
644 <https://doi.org/10.5281/zenodo.1045297>, 2017a.

645 Petersson, N. A. and Sjogreen, B.: User’s guide to SW4, version 2.0, LLNL-SM-741439., [https://doi.org/.](https://doi.org/),  
646 2017b.

647 Pitarka, A., Akinci, A., De Gori, P., and Buttinelli, M.: Deterministic 3D Ground-Motion Simulations (0–5 Hz)  
648 and Surface Topography Effects of the 30 October 2016 Mw 6.5 Norcia, Italy, Earthquake, *Bull. Seismol. Soc.*  
649 *Am.*, <https://doi.org/10.1785/0120210133>, 2021.

650 Rosenthal, M., Ben-Avraham, Z., and Schattner, U.: Almost a sharp cut – A case study of the cross point  
651 between a continental transform and a rift, based on 3D gravity modeling, 761, 46–64,  
652 <https://doi.org/10.1016/j.tecto.2019.04.012>, 2019.

653 Rybakov, M., Fleischer, L., and ten Brink, U.: The Hula Valley subsurface structure inferred from gravity data,  
654 *Isr. J. Earth Sci.*, 52, 113–122, <https://doi.org/10.1560/WF6V-4BVG-GXQM-PKVR>, 2003.

655 Sadeh, M., Hamiel, Y., Ziv, A., Bock, Y., Fang, P., and Wdowinski, S.: Crustal deformation along the Dead Sea  
656 Transform and the Carmel Fault inferred from 12 years of GPS measurements, *J. Geophys. Res. Solid Earth*,  
657 117, <https://doi.org/10.1029/2012JB009241>, 2012.

658 Shamir, G., Bartov, Y., Sneh, A., Fleisher, L., Arad, V., and Rosensaft, M.: Preliminary seismic zonation in

659 Israel, earthquake.co.il<sup>28</sup> , pp., 2001.

660 Shani-Kadmiel, S., Tsesarsky, M., and Gvirtzman, Z.: Distributed slip model for forward modeling strong  
661 Earthquakes, *Bull. Seismol. Soc. Am.*, 106, 93–103, <https://doi.org/10.1785/0120150102>, 2016.

662 Shani-Kadmiel, S., Volk, O., Gvirtzman, Z., and Tsesarsky, M.: Ground motion amplification atop the complex  
663 sedimentary basin of Haifa Bay (Israel), *Bull. Earthq. Eng.*, 18, 821–836, [https://doi.org/10.1007/s10518-018-](https://doi.org/10.1007/s10518-018-00533-9)  
664 00533-9, 2020.

665 Shi, Z. and Ben-Zion, Y.: Dynamic rupture on a bimaterial interface governed by slip-weakening friction,  
666 *Geophys. J. Int.*, 165, 469–484, <https://doi.org/10.1111/j.1365-246X.2006.02853.x>, 2006.

667 Shimony, R., Gvirtzman, Z., and Tsesarsky, M.: Seismic energy release from intra-basin sources along the dead  
668 sea transform and its influence on regional ground motions, *Bull. Seismol. Soc. Am.*, 111, 295–308,  
669 <https://doi.org/10.1785/0120200215>, 2021.

670 Volk, O., Shani-Kadmiel, S., Gvirtzman, Z., and Tsesarsky, M.: 3D effects of sedimentary wedges and  
671 subsurface canyons: Ground-motion amplification in the Israeli coastal plain, *Bull. Seismol. Soc. Am.*, 107,  
672 1324–1335, <https://doi.org/10.1785/0120160349>, 2017.

673 Wald, D. J., Quitoriano, V., Heaton, T. H., and Kanamori, H.: Relationships between peak ground acceleration,  
674 peak ground velocity, and modified mercalli intensity in California, *Earthq. Spectra*, 15, 557–564,  
675 <https://doi.org/10.1193/1.1586058>, 1999.

676 Walling, M. . and Abrahamson, N. .: Non-Ergodic Probabilistic Seismic Hazard Analyses, in: 15th World  
677 Conference on Earthquake Engineering (15WCEE). Lisbon, Portugal, 24-28 September, 2012.

678 Wang, Z.: A Clear Definition of Seismic Hazard and Risk: A Basis for Hazard and Risk Assessment,  
679 *Communication, and Management*, *Am. Geophys. Union*, 2005, S53B-1110, 2005.

680 Wells, D. L. and Coppersmith, K. J.: New empirical relationships among magnitude, rupture length, rupture  
681 width, rupture area, and surface displacement, *Bull. - Seismol. Soc. Am.*, 84, 974–1002, 1994.

682 Wetzler, N. and Kurzon, I.: The earthquake activity of Israel: Revisiting 30 years of local and regional seismic  
683 records along the dead sea transform, *Seismol. Res. Lett.*, 87, 47–58, <https://doi.org/10.1785/0220150157>, 2016.

684 Yagoda-Biran, G., Maiti, S. K., Wetzler, N., Nof, R. N., Pashcur, Y., and Kamai, R.: A ground-motion database  
685 for Israel with its corresponding point-source parameters, for engineering seismology applications, *Seismol.*  
686 *Res. Lett.*, 92, 2679–2690, <https://doi.org/10.1785/0220200477>, 2021.

687 Zohar, M.: Temporal and spatial patterns of seismic activity associated with the Dead Sea transform (DST)  
688 during the past 3000 yr, *Seismol. Res. Lett.*, 91, 207–221, <https://doi.org/10.1785/0220190124>, 2019.

689